# Transonic buffet alleviation via virtual control surfaces

Andrea Petrocchi [a], Mariadebora Mauriello [b], George Barakos [a],*

[a] *CFD Laboratory, School of Engineering, University of Glasgow, Glasgow, G128QQ, UK*
[b] *Aix Marseille Université, CNRS, IUSTI, Marseille, France*

## ARTICLE INFO

## ABSTRACT

In this work, computational fluid dynamics simulations are carried out to assess the ability of control surfaces to alleviate or suppress transonic buffet. Among the available control surfaces, upper trailing edge flaps were considered since they modify the aerofoil pressure distribution and fix the shock at an upstream position. Spoilers were also studied as they produce a similar effect by interfering with the pressure disturbance propagation in the boundary layer and prevent buffet. For both devices, the sensitivities to geometric parameters are studied. The effectiveness of these buffet control methods is first assessed for 2D computations around different wing sections. As spoilers were considered more effective, results on a 3D configuration are provided to discuss the influence of finite-span devices on aerodynamic performance. In addition, a simple model accounting for changes in the flight Mach number together with the spoiler is presented to simulate a simple flight scenario and provide an effective strategy for buffet suppression. In the framework of numerical investigations, the adoption of virtual control surfaces allows for avoiding difficulties associated with the modelling of slotted and deployable devices.

## 1. Introduction

At transonic flow conditions, shock wave/boundary layer interaction and the induced, unsteady flow separation lead to a phenomenon known as buffet. It consists of self-sustained shock oscillations around aerofoils and wings. Since the middle of the last century, several experimental and numerical studies have been conducted to shed light on the mechanism driving the shock oscillations [1–5]. Buffet has consequences on the structural aircraft response as it can lead to structural fatigue. Moreover, it deteriorates the aircraft handling qualities and can also cause passenger discomfort in flight. Therefore, an airplane must be free from oscillations at any operating conditions and a buffet boundary is part of the flight envelope boundary. Nonetheless, variations of the flight conditions due to gusts or emergency maneuvers may cause the plane to cross the buffet boundary and undergo buffet. Therefore, in recent years, increasing attention has been paid to control methods to eliminate or alleviate shock-induced oscillations (SIO).

The work of Giannelis et al. [6] provides a partial review of flow control works for buffet. The employed techniques mainly distinguish into vortex generators (VGs) [7–9], shock-control bumps (SCB) [10–13] and trailing edge devices (TED) [14–17]. VGs help alleviate buffet by energising the downstream boundary layer and making it less prone to separation [18]. SCBs aim at smearing the shock and reducing pressure losses across it. If correctly placed, they help fix the shock position. The main drawback lies in the correct positioning of these devices. Both 2D and 3D configurations, i.e. infinite and spanwise finite, respectively, must be accurately placed to provide good results [19]. TEDs aim to reduce the pressure jump across the shock, the shock intensity, and the probabilities of separation. In this category, we find trailing edge deflectors, trailing edge flaps and Gurney flaps.

All methods proved to be more or less able to eliminate the shock oscillations at design conditions. Unfortunately, the first two categories of devices introduce installation drag, deteriorating the aerodynamic performance in cruise. To minimise drag penalties, expensive, and sometimes unsuccessful, works of optimization involving shape, number, and position of the devices are required. If such studies can be carried out for simple configurations [20,21], they are overly expensive for full-wing geometries.

This paper presents some alternatives to the aforementioned methods by taking advantage of existing control surfaces available in most airplanes. Recently, attention has been paid to three-dimensional buffets, and both experimental [22–24] and numerical [25–28] studies have been conducted. The numerical study of Iovnovich and Raveh [25] first identified the presence of spanwise-propagating waves called *buffet cells*. These structures exhibit the

* Corresponding author.
*E-mail addresses:* andrea.petrocchi@glasgow.ac.uk (A. Petrocchi),
mariadebora.mauriello@univ-amu.fr (M. Mauriello), george.barakos@glasgow.ac.uk
(G. Barakos).

**Nomenclature**

Latin Symbols

| | | |
|---|---|---|
| $b$ | wingspan | m |
| $c$ | aerofoil chord | m |
| $C_p$ | pressure coefficient $(p - p_\infty)/(0.5\rho U_\infty^2)$ | |
| $C_D$ | drag coefficient $D/(0.5\rho U_\infty^2 cb)$ | |
| $C_L$ | lift coefficient $L/(0.5\rho U_\infty^2 cb)$ | |
| $C_\mu$ | model constant | |
| $f_k$ | unresolved-to-total ratio of turbulent kinetic energy | |
| $f_\epsilon$ | unresolved-to-total ratio of turbulent dissipation | |
| $f_\omega$ | unresolved-to-total ratio of turbulent frequency | |
| $F_1$, $F_2$ | SST model blending functions | |
| $k$ | turbulent kinetic energy | $\mathrm{m^2\,s^{-2}}$ |
| $L_G$ | Gurney length | m |
| $L_{\mathrm{UTEF}}$ | UTEF length | m |
| $\mathrm{M}_\infty$ | Mach number | |
| $N_{\mathrm{act}}$ | Number of steps required for the actuation | |
| $P_k$ | turbulent kinetic energy production term | $\mathrm{kg\,m^{-1}\,s^{-3}}$ |
| $\mathbf{R}$ | flow residual vector | |
| $\mathrm{Re}_c$ | Reynolds number $\rho U_\infty c/\mu$ | |
| $t$ | time | s |
| $T_{\mathrm{off}}$ | device retraction time | s |
| $U_i$ | flow velocity | $\mathrm{m\,s^{-1}}$ |
| $V_{i,j,k}$ | cell volume | |
| $x_i$ | spatial coordinates | m |
| $\mathbf{X}$ | grid position | m |
| $\dot{\mathbf{X}}$ | grid velocity | $\mathrm{m\,s^{-1}}$ |
| $\ddot{\mathbf{X}}$ | grid acceleration | $\mathrm{m\,s^{-2}}$ |
| $\mathbf{W}$ | flow variable vector | |
| $\alpha$ | angle of attack | deg |

Greek Symbols

| | | |
|---|---|---|
| $\delta_s$ | spoiler deflection angle | deg |

| | | |
|---|---|---|
| $\Delta t$ | timestep | s |
| $\Delta t_{\mathrm{act}}$ | device time of deployment | s |
| $\dot{\delta}_s$ | spoiler deflection rate | deg/s |
| $\mu$ | molecular dynamic viscosity | $\mathrm{kg\,m^{-1}\,s^{-1}}$ |
| $\mu_t$ | eddy viscosity | $\mathrm{kg\,m^{-1}\,s^{-1}}$ |
| $\nu_t$ | kinematic eddy viscosity | $\mathrm{m^2\,s^{-1}}$ |
| $\omega$ | turbulent frequency | $\mathrm{s^{-1}}$ |
| $\rho$ | density | $\mathrm{kg\,m^{-3}}$ |
| $\beta^*$, $\beta$, $\gamma$, $\sigma_k$, $\sigma_\omega$ | SST model constants | |

Acronyms

| | |
|---|---|
| BILU | Block Incomplete Lower-Upper |
| CFD | Computational Fluid Dynamics |
| DDES | Delayed Detached-Eddy Simulations |
| DES | Detached-Eddy Simulations |
| GCG | Generalized Conjugate Gradient |
| GMRES | Generalized Minimum Residual |
| HMB | Helicopter Multi-Block |
| IDDES | Improved Delayed Detached-Eddy Simulations |
| LES | Large-Eddy Simulations |
| MUSCL | Monotone Upstream-centered Scheme for Conservation Laws |
| PANS | Partially Averaged Navier-Stokes |
| RANS | Reynolds-Averaged Navier-Stokes |
| SAS | Scale-Adaptive Simulations |
| SCB | Shock-Control Bumps |
| SIO | Shock-Induced Oscillation |
| SST | Shear Stress Tensor |
| TED | Trailing Edge Devices |
| URANS | Unsteady Reynolds-Averaged Navier-Stokes |
| UTEF | Upper Trailing Edge Flap |
| VG | Vortex Generator |

alternation of positive and negative pressure disturbances mostly propagating toward the wing tip. The presence of buffet cells represents one of the main differences with respect to 2D cases and was experimentally verified by subsequent studies [22–24]. The literature on conventional 3D transonic wings locates buffet cells around 45-60% of the wingspan [29,26,27,24]. Therefore, spoilers can find application for buffet alleviation. Upper trailing edge flap (UTEF) and Gurney flaps represent a valid alternative to spoilers as they can be easily implemented and deployed only when required.

UTEFs act at the trailing edge by enforcing separation. The local angle of attack reduction results in a more upstream shock position. The weaker shock no longer (or mildly) separates the boundary layer. Under this condition, the shock foot (if present) and trailing edge separated flow regions cannot merge and buffet is suppressed. The work of Tian et al. [17] showed the ability of UTEFs to cancel buffet around the RAE2822 aerofoil by altering the aerofoil chamber and curvature. The addition of the UTEF allows a delay in the onset of buffet but induces a reduction of lift at both pre- and post- onset by shifting the shock upstream and reducing the flow acceleration at the leading edge and the suction peak. Therefore, in our view, the use of such devices must be limited to buffet conditions. The results of Tian et al. [17] were partially confirmed by the experimental investigation of D'Aguanno et al. [30] on the OAT15A. The use of a 1-2%$c$ UTEF showed increasing efficiency in alleviating buffet, without suppressing it completely.

On the other hand, the use of spoilers alters the state of the boundary layer and the buffet phenomenon can be interrupted

according to the most popular buffet mechanisms. The acoustic feedback mechanism of Lee [3] sees the downstream propagation of disturbances generated at the shock foot in the boundary layer. Upon reaching the trailing edge, other upstream propagating waves are generated. These latter travel in the subsonic flow above the boundary layer and feed the shock motion, completing a feedback loop that allows for the self-sustained shock motion. This mechanism was further investigated by several authors [31,32] who confirmed the central role of upstream-travelling acoustic waves in feeding the shock motion. Instead, the works from Crouch et al. [33,5] and following works ([34,27] among the others) studied transonic buffet as a global flow instability. In these works, buffet is seen as the result of a first unstable mode, involving the entire flow field. In both cases, the propagation of disturbances in the boundary layer is crucial. Whether one or the other explanation is preferred, the use of spoilers in hampering the mechanism seems reasonable. A sketch of the working principle compared to the mechanism of Lee [3] is given in Fig. 1. The spoiler deployment (see Fig. 1, right) generates fixed point separation at the device tip, resulting in an increase in the wing camber and a local reduction of the angle of attack. The shock is pushed upstream where it loses intensity and eventually no longer separates the boundary layer. If the boundary layer still separates, the spoiler obstacles the merging of the trailing edge and shock foot separation regions, alleviating or suppressing the SIO. Retracted in the wing, spoilers do not introduce installation drag nor off-design penalties like VGs or SCBs [35]. When buffet is detected, spoilers are deployed to reduce and/or suppress the SIO. An overview of adaptive concepts
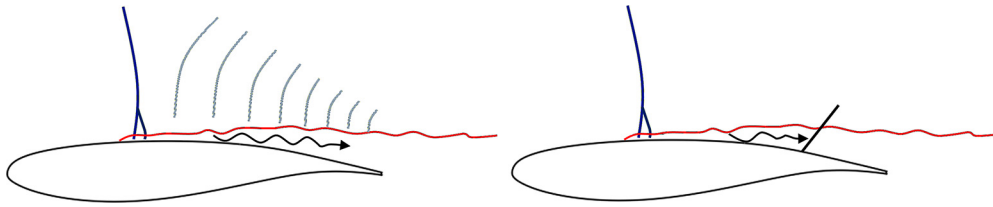
**Fig. 1.** Left: sketch of the acoustic feedback mechanism of Lee [3]; right: effect of the spoiler in stopping the downstream propagation of disturbances in the boundary-layer.

for shock control is given in the review paper of Künnecke et al. [36].

Tian et al. [37] performed numerical simulations by modelling spoilers with a thickening of the aerofoil/wing sections between 80% of the chord and the trailing edge. The results were encouraging on both 2D and 3D configurations, since the buffet onset was delayed. The thicker trailing edge resulted in an upstream position of the shock. This helps delay buffet at higher angles of attack or Mach numbers. In their work, the hypothesis of separated flow behind the spoiler allowed for the aforementioned approach, consisting of a simple thickening of the aerofoil. This approach does not account for changes in sizes of the separated region behind the spoiler nor for flow re-attachment in case of small spoiler deployments. Moreover, a change in the spoiler angle would require a modification of the mesh. At pre-buffet conditions, the presence of the spoiler causes an increase in the aerofoil chamber and causes the shock to move upstream, resulting in losses of lift. Therefore, to avoid undesired effects associated with the presence of control devices at non-buffet conditions, they must be only deployed under buffet conditions.

In the computational fluid dynamics (CFD) framework, the position of all control devices within the wing and their mobility result in difficulties in modelling both trailing edge flaps and spoilers. The aforementioned CFD works only accounted for the presence of fixed controlled devices. In this work, the technique of Pastrikakis and Barakos [38] is adopted to simulate virtual control surfaces. The technique works on cell faces to simulate the presence of no-slip walls. Without using a moving grid, this method allows studying the flow response to different angles of spoiler deployment and UTEF length and reproducing a dynamical deployment of the control surfaces. The ability to vary the position and extent of deployable control devices over time opens the door to closed-loop control on wings by means of the aforementioned strategies. Nonetheless, in this work, only a demonstration of automatic deployment and retraction is given.

The paper is structured as follows: the mathematical model is presented in section 2. There, attention is paid to the control surface modelling and the actuation strategy; in section 3 test cases and numerical setup are described; section 4 is devoted to flow control application. The method is first tested for 2D configurations with upper trailing edge, Gurney flaps, and spoilers. The influence of the test section is presented by comparing the results of 2D computations for the flow around different aerofoils with activated control surfaces. The sensitivity to the spoiler deflection angle and the UTEF length is studied. For a selected case, the spoiler deployment was complemented with a decrease in Mach number to simulate the pilot action in a flight scenario. Among the pool of spoiler angles considered, the optimal value and a different, higher, one were tested on a 3D configuration with a finite wingspan to underline differences between the 2D and 3D cases; section 5 is devoted to discussion and conclusions.

## 2. Numerical method

### 2.1. Computational model for fluid flow

Numerical simulations have been performed using the Helicopter Multi-Block (HMB3) [39,40] flow solver, a three-dimensional, fully implicit, structured, code for the solution of the Navier-Stokes equations. The Navier-Stokes equations are discretised using a cell-centered finite volume approach. The computational domain is divided into a finite number of non-overlapping control volumes, and the governing equations are applied to each cell in turn. Also, the Navier-Stokes equations are re-written in a curvilinear co-ordinate system which simplifies the formulation of the discretised terms since body-conforming grids are adopted here. The spatial discretisation of the equations leads to a set of ordinary differential equations in time,

$$\frac{\mathrm{d}}{\mathrm{d}t}(\mathbf{W}_{ijk}V_{ijk}) = -\mathbf{R}_{ijk}(\mathbf{W}), \tag{1}$$

where $\mathbf{W}$ and $\mathbf{R}$ are the vectors of cell conserved variables and residuals respectively, and $V$ is the cell volume. The convective terms are discretised using Osher's upwind scheme [41]. A monotone upstream-centered scheme for conservation laws (MUSCL) variable extrapolation [42] is used to provide second-order accuracy with the Van Albada limiter [43] to prevent spurious oscillations around shock waves. For the integration in time, the implicit dual-time stepping method of Jameson [44] is used.

The linearised system of equations is solved using the generalised conjugate gradient (GCG) method with a block incomplete lower–upper (BILU) factorisation as a pre-conditioner [45]. The Jacobian is approximated by evaluating the derivatives of the residuals with a first-order scheme for the inviscid fluxes. The first-order Jacobian requires less storage and ensures a better convergence rate to the GCG iterations. The steady-state solver for turbulent flows is formulated and solved in an identical manner to that of the mean flow. The eddy-viscosity is calculated from the latest values of the turbulent variables, e.g. $k$ and $\omega$, and is used to advance the mean and the turbulent flow solutions. An approximate Jacobian is used for the source term of the models by only taking into account the contribution of their dissipation terms, i.e. no account of the production terms is taken on the left-hand side of the system. The solver offers several one-, two-, three-, and four-equation turbulence models. In addition, LES, DES, delayed DES (DDES), improved DDES (IDDES), SAS and PANS methods are also available.

### 2.2. PANS formulation

The partially-averaged Navier-Stokes (PANS) formulation [46] is a bridging model between RANS and DNS. The formulation is based on a RANS paradigm, where the blending is obtained by means of the user-prescribed unresolved-to-total ratios of turbulent kinetic energy $f_k$ and dissipation $f_\epsilon$, bounded between 0 and 1, acting on the turbulence closure equations. They read: $f_k = k_u/k$, $f_\epsilon = \epsilon_u/\epsilon$, where the $u$ subscripts stand for unresolved and

the quantities at the denominator are the total ones. The PANS method was initially derived for k-$\epsilon$ closures and then extended to the Wilcox k-$\omega$ model [47] by Lakshmipathy et al. [48] and to the Menter SST model [49] by Luo et al. [50]. In k-$\omega$ based formulations the parameter $f_\epsilon$ is replaced by the unresolved-to-total turbulence frequency $f_\omega = \omega_u/\omega = f_\epsilon/f_k$. These formulations inherit from the parent RANS models an eddy viscosity based on a Boussinesq approximation, that is reduced with respect to the RANS case because of the effects of the $f_k$ parameter: since only a fraction of the turbulent kinetic energy is modelled, the corresponding value of the eddy viscosity is reduced. This gives the possibility for the turbulent structures to be resolved. When adopting a reasonably high value of $f_k$ the method can be used as a less dissipative version of URANS.

In this work the SST-PANS formulation is adopted. It reads:

$$\frac{\partial(\rho k)}{\partial t} + \frac{\partial(\rho U_j k)}{\partial x_j} = P_k - \beta^* \rho k \omega + \frac{\partial}{\partial x_j}\left[\left(\mu + \mu_t \sigma_k \frac{f_\omega}{f_k}\right)\frac{\partial k}{\partial x_j}\right],$$
(2)

$$\frac{\partial(\rho\omega)}{\partial t} + \frac{\partial(\rho U_j \omega)}{\partial x_j} = \frac{\gamma}{\nu_t} P_k - \beta' \rho \omega^2$$
$$+ \frac{\partial}{\partial x_j}\left[\left(\mu + \mu_t \sigma_\omega \frac{f_\omega}{f_k}\right)\frac{\partial\omega}{\partial x_j}\right]$$
$$+ 2\frac{f_\omega}{f_k}(1 - F_1)\frac{\rho \sigma_{\omega 2}}{\omega}\frac{\partial k}{\partial x_j}\frac{\partial\omega}{\partial x_j},$$
(3)

where $\rho$ is the density, $U_j$ is the flow velocity, $\mu$ is the dynamic molecular viscosity and $\mu_t$ is the turbulent viscosity. Here, the turbulent kinetic energy $k$ and frequency $\omega$ are the modelled, or unresolved, fraction where the subscripts were dropped for sake of simplicity. In the $\omega$-equation, $\beta' = \left(\gamma \beta^* - \frac{\gamma \beta^*}{f_\omega} + \frac{\beta}{f_\omega}\right)$; $F_1$ is the blending function while $\gamma, \beta, \beta*, \sigma_k, \sigma_\omega$ are the model constants, calculated as prescribed in reference [49]. The eddy viscosity has the same form as in the formulation of the SST model.

## 2.3. Virtual control surface modelling

### 2.3.1. Gurney flaps/UTEF

In HMB3, Gurney flaps and UTEF can be modelled either by an *ad-hoc* multi-block grid or virtually. As the first strategy makes difficult to simulate an actuation, the second method is preferred. The method adopted in this work was formulated in [51] and here it is briefly discussed. The flap is located along a block face (see Fig. 2) of the multi-block grid by defining a planar surface with three points. At each iteration, the length of the flap is updated according to a temporal, user-prescribed law and only part of the plane is accounted for. In each block, cells faces coinciding with block faces are flagged if their distance from the flap plane and their orientation with respect to the plane falls within a user-prescribed tolerance. If the projection of a cell face does not fall entirely in the defined plane, the cell is only flagged if its centroid projection falls onto the plane. Cells which do not satisfy those requirements are discarded, while no-slip boundary conditions are imposed on the flagged cells. The algorithm to identify Gurney/UTEF cell faces is repeated in Algorithm 1.

Fig. 2, right images, shows the location of an UTEF at the initial (top) and final (bottom) instants of the actuation. The number of flagged cells is modified at each timestep according to the specified temporal law of actuation. In Fig. 2, the portion of the block boundary occupied by the control surface is indicated by the change in colour. Using this method, it is only important to place a block boundary at a convenient position to represent the control surface.

### 2.3.2. Spoilers

Virtual spoilers are modelled following the implementation in HMB3 of Pastrikakis and Barakos [38] for swinging Gurney flaps. In Fig. 3, left image, the mesh adopted around the OAT15A aerofoil with virtual spoilers is shown. To build such a grid around the spoiler location, a hinge (see. Fig. 3, right images) must be introduced. Using this grid topology, the virtual spoiler can be simulated by flagging the nearest cell faces at its instantaneous position as boundary faces, and imposing no-slip boundary conditions. Adopting this method, once the grid is properly built, no additional effort is required in terms of mesh generation, and the moving surface can be modelled without the need for overset or overly fine grids. Fig. 3, right images, shows a close view of the hinge location with the deployed spoiler. No-slip boundary conditions are imposed on the red cell faces. Given the multi-block nature of the solver, the user can specify within which blocks the spoiler is contained. In Fig. 3, the two rightmost blocks around the hinge are flagged as *spoiler blocks*, and the spoiler cannot be deployed more than, roughly, 90 degrees from its initial position. As for the UTEF/Gurney flaps, the spoiler position is given in input by specifying three points corresponding to the beginning and end of the hinge and a third point to define the spoiler plane. For quasi-2D configurations (an application will be shown in section 4.4), the first two points determine the spanwise extent of the spoiler, while the third determines the spoiler length. Once the initial spoiler position is calculated, it can be deployed by following a linear law or a temporal law based on a summation of harmonics.

To determine the instantaneous spoiler position and the corresponding boundary flags, we use the algorithm of [51], repeated here in Algorithm 2.

### 2.3.3. Automatic deployment of the control devices

Buffet control by means of control surfaces could be made automatic by using probes in the boundary layer to detect separation. At design conditions, flow separation (if any) takes place at the shock foot, while in buffet regimes the separated flow region extends, during a fraction of the buffet period, from the shock foot to the trailing edge. In this view, the idea is to place a sensor in the boundary layer at a strategic location, i.e. where separation is not expected in cruise (design) conditions, and exploits the information at that point to activate flow control when required.

The sketch in Fig. 4, left images, illustrates the control point for buffet detection for an aerofoil with spoiler. The same actuation can be adopted for the UTEF case. The probe located on the aerofoil surface at a specified location ($x/c = 0.7$ in figure) samples the conserved flow variables at each timestep. The printed values are the ones at a distance $\Delta y/2$ from the wall, being $\Delta y$ the normal spacing of the first cell. When flow reversal is detected the spoiler is deployed following a linear law:

$$\delta_s = \delta_{s,0} + \min(\dot{\delta_s}(t - t_{B,0}), \delta_{s,\max}),$$
(4)

where $\delta_{s,0}$ is the position of the undeployed spoiler, $\dot{\delta_s}$ is the user-described angular velocity, assumed constant over the spoiler excursion, and $\delta_{s,\max}$ is the maximum displacement. We indicated with $t_{B,0}$ the instance when buffet is first detected. In the solver, this is implemented by applying a discrete increment for each timestep:

$$\delta_s^i = \delta_{s,0} + \min(\dot{\delta_s}(i\Delta t - t_{B,0}), \delta_{s,\max}), \quad \dot{\delta_s} = \delta_{s,\max}\Delta t_{act},$$
$$\Delta t_{act} = 1/N_{act},$$
(5)

where the velocity is specified by means of the parameter $\Delta t_{act}$, equal to the inverse of the number of unsteady steps required to deploy the device $N_{act}$. A demonstration will be given in section 4.

**Algorithm 1** Pseudo-code for Gurney flaps/UTEF definition. From [51].

---

Data: Define the Gurney as a set of points
**for all the** blocks in the mesh **do**
    **for all the** internal boundaries of each block **do**
        **for all the** faces on each internal boundary **do**
            **if** the centroid of the face is close to the Gurney/UTEF **then**
                **if** the normal to the Gurney/UTEF is nearly parallel to the normal of the face **then**
                    **if** the centroid of the face is inside the polygon of the Gurney/UTEF **then**
                        Flag this face as in the Gurney/UTEF
                    **end if**
                **end if**
            **end if**
        **end for**
    **end for**
**end for**
All the cell faces up to that node will be flagged as boundary cells

---
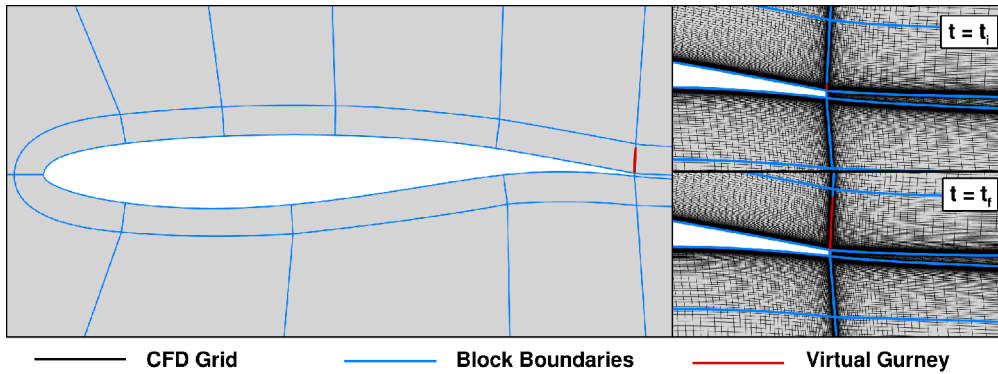


**Fig. 2.** Left: multi-block grid topology around the OAT15A aerofoil; right: grid around the trailing edge at the initial (top) and final (bottom) instants of the UTEF deployment. (For interpretation of the colours in the figure(s), the reader is referred to the web version of this article.)
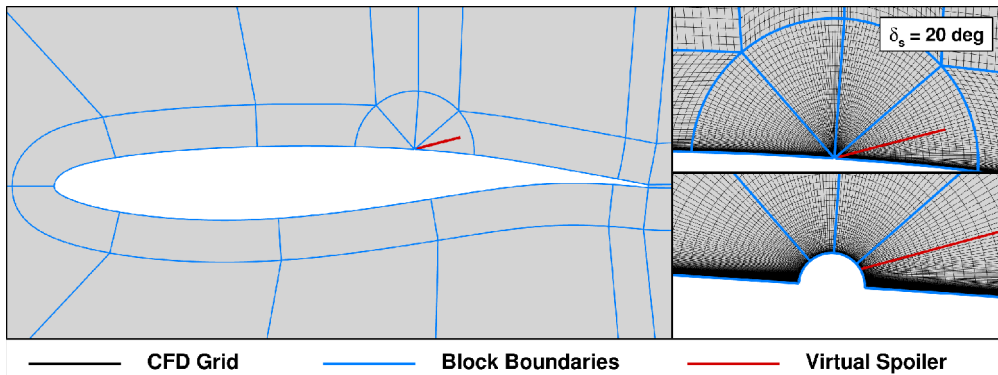


**Fig. 3.** Left: multi-block grid topology around the OAT15A aerofoil with virtual spoiler; right: grid around the spoiler hinge for a spoiler angle deflection of 20 deg.
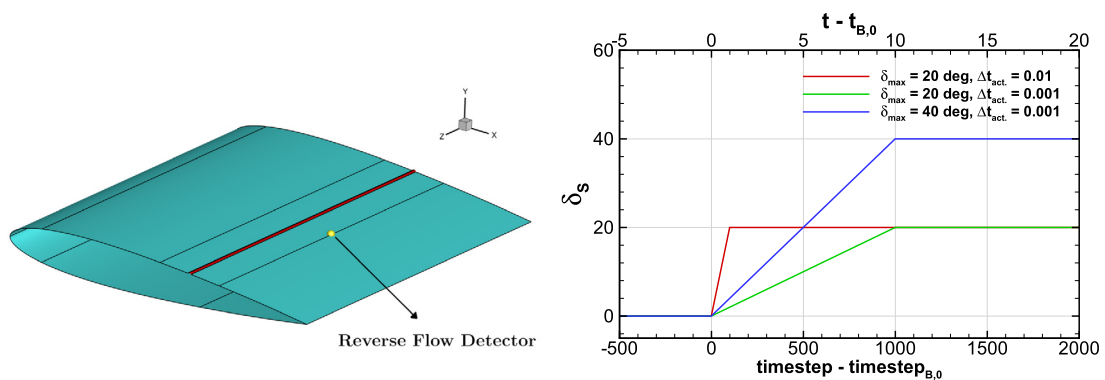


**Fig. 4.** Right: sketch of the buffet sensor employed around a NACA0012 aerofoil. Black lines represent surface block boundary while the red surface indicates the hinge; left: spoiler angle versus time for different value of the parameters $\Delta t_{act}$ and $\delta_{s,max}$.
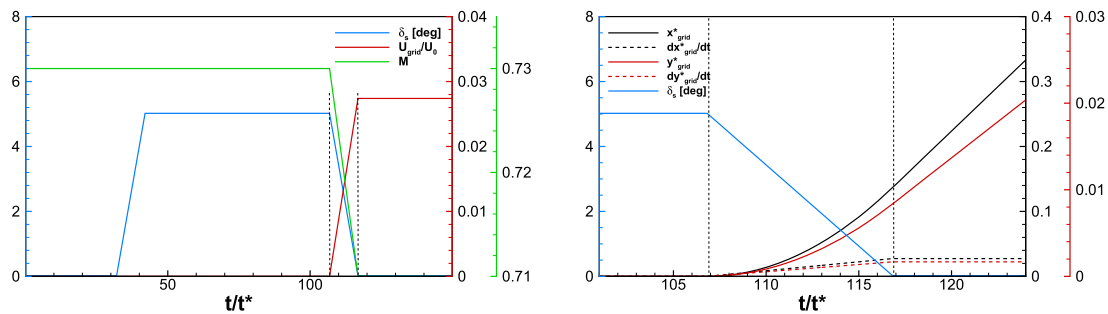
**Fig. 5.** Left: time trend of the Mach number in response to the grid velocity. Right: instantaneous x and y components of position and velocity vectors within the spoiler retraction time window.

---

**Algorithm 2** Pseudo-code for spoiler definition.

Find the spoiler size
Find the spoiler angle
**for all** *spoiler blocks* in the mesh **do**
   **if** the point is inside the radius **then**
      Flag the cells behind and in front of the spoiler with -1 and 1
   **else**
      Flag the cells behind and in front of the spoiler with -2 and 2
   **end if**
**end for**
Sweep along the lines
**if** the sign changes between two cells **then**
   **if** the sum of the four neighbour cells of a node is 6 **then**
      This node is the end of the spoiler
   **end if**
**end if**
All the cell faces up to that node will be flagged as boundary cells

---

Fig. 4, right image, shows the temporal laws corresponding to different values of $\delta_{s,\max}$ and $\Delta t_{act}$. The device retraction follows the same linear behaviour shown in eq. (5). As the deployment of a control surface generates separation on the airfoil, the presence of reversed flow is no longer a valuable buffet indicator. Therefore, the spoiler retraction, when necessary, is applied at an arbitrary time. It must be pointed out that dynamic control based on observables is beyond the scope of this work. Nevertheless, a smooth deployment and retraction of the control devices allows for a more plausible description of the control dynamics and avoids abrupt changes in the flow field due to the appearance/disappearance of the control surfaces.

### 2.3.4. Changing flow conditions with grid motion

Regardless of their ability to suppress buffet, slotted flow control surfaces are likely to introduce drag penalties or non-equilibrium in lift and pitching moment (for 2D and quasi-2D configurations). Therefore, the devices must be retracted to avoid such penalties for a long period of time. If the flow conditions do not vary after the application of flow control, SIO will take place again. To prevent this, the pilot (or the automatic control system) will act to return to flight conditions below the buffet boundary by reducing the flight speed, the angle of attack, or both. Hence, while the control surface temporarily suppresses buffet, a change in flight conditions will prevent the appearance of new oscillations. To account for such an action, in this work, we simulated a reduction of the Mach number by moving the entire CFD grid. A positive (negative) grid velocity $U_{grid}$ aligned with the free stream velocity will result in a reduced (increased) local flow velocity, i.e. Mach number. Fig. 5, left plot, shows the control strategy adopted. The spoiler (blue lines in figure) is first deployed following eq. (5), and, after the SIO is stopped, it is retracted within an equal time window. At the same time, the grid is put in motion with constant acceleration until the spoiler is retracted. At this point, the local Mach number (green line) is such to avoid the occurrence of

buffet. Given the initial and final Mach numbers $M_{\infty,0}$ and $M_{\infty,F}$, respectively, the grid acceleration, velocity and displacement can be written as:

$$\ddot{\mathbf{X}} = \frac{\mathbf{U}_\infty \left( \frac{M_{\infty,F}}{M_{\infty,0}} - 1 \right)}{T_{\text{off}}}, \quad \dot{\mathbf{X}} = \max(\ddot{\mathbf{X}}t', \dot{\mathbf{X}}_{\max}), \quad \mathbf{X} = \dot{\mathbf{X}}t' + \frac{1}{2}\ddot{\mathbf{X}}t'^2, \tag{6}$$

where $t' = t - t_{\text{off},i}$ is the time from the beginning of the spoiler retraction. The time windows of the spoiler retraction ($T_{\text{off}}$) and the aerofoil deceleration might be selected to have different lengths and locations in time. Nevertheless, in this work, the two actions will be simultaneous. The right plot in Fig. 5 shows the $x-$ and $y-$components of the grid velocity and position within the spoiler retraction time window. The $x-$ and $y-$components are obtained by projecting the $\ddot{\mathbf{X}}$, $\dot{\mathbf{X}}$, $\mathbf{X}$ onto the parallel and perpendicular direction of the free stream velocity, i.e. by multiplying by $\cos(\alpha)$ and $\sin(\alpha)$, respectively. In this paper, an application is shown in conjunction with spoilers in section 4.3.3, but might be used with any deployable flow control surface.

## 3. Test case description and numerical setup

### OAT15A wing section

The first configuration of interest is the supercritical OAT15A wing section, experimentally investigated in the S3Ch wind tunnel at ONERA [52,4]. The chord and span of the experimental wing model were $c = 0.23$ m and 0.78 m, respectively, the latter coinciding with the extent of the wind tunnel facility. The section had a thickness-to-chord ratio of $t/c = 0.123$ and a trailing edge thickness of 0.5% of the chord. The wing was mounted in an orthogonal section wind tunnel having nominal dimensions of 0.78 m × 0.78 m × 2.2 m. Measurements were collected at free-stream Mach numbers in the range of 0.7-0.75, a chord-based Reynolds number of $\text{Re}_c = 3 \times 10^6$ and angle of attack in the range of 1.36 - 3.9 deg. Static and dynamic pressure measurements allowed for the detection of buffet at an angle of attack of 3.1 deg at $M_\infty = 0.73$ and 3.5 deg at $M_\infty = 0.72$. For the case at $M_\infty = 0.73$ and $\alpha = 3.5$ deg, velocity-field data were also acquired to compute statistics. Although a large characterisation of the buffet onset was not provided at all flow conditions, the available data ware used to assess the accuracy of the time-marching simulations for the documented buffet flow. In this work, simulations at $\text{Re}_c = 3 \times 10^6$, $M_\infty = 0.73$ and $\alpha = 3.5$ deg were carried out.

### NACA0012 wing section

The second test section analysed is the NACA0012 section. It was studied at the Ames High Reynolds Number Facility by McDevitt and Okuno [53]. Mach numbers were in the range of 0.71-0.8 and Reynolds number spanned between 1 and 10 million. The buffet onset was detected by means of steady and unsteady pressure

measurements. The tunnel walls were adapted to follow the free air streamlines, while the sidewall interference was reduced by thinning the sidewall boundary layer by means of suction applied on porous panels. Further details are given in the reference. Although these experiments are more than 30 years old, they still represent the broadest database for buffet onset, covering a wide range of conditions. Moreover, the treatment of the wind tunnel wall allowed to consider the flow as close as possible to 2D, making this test case particularly suitable for this study. Here, simulations at $Re_c = 10 \times 10^6$, $M_\infty = 0.72$ and $\alpha = 6.0$ deg ($\simeq 2.0$ deg above the onset) were carried out.

*V2C wing section*

The last configuration is the V2C aerofoil of Dassault Aviation, studied during the European project TFAST [54]. It is a laminar type supercritical aerofoil designed to operate between Mach numbers of 0.7 and 0.75 and was studied in the Trisonic wind tunnel of the Polish Institute of Aviation. The tunnel is $0.6 \times 0.6$ m in section and it was equipped with 1.58 m long solid walls deflected 0.5 deg from each other. The model chord was 0.2 m, the span was 0.6 m, and the relative thickness was 15%. A transition strip - of varying height - was added on the upper side and tested at several streamwise positions and fixed along the wingspan. The mean value of static pressure on the V2C profile was measured by means of a 64 pressure tab system connected to tubes mounted inside the model, grouped in two rows. An aerodynamic rake was used to estimate the drag. Kulite pressure transducers were used to measure unsteady pressure in the vicinity of the shock, while SEN-FLEX sensors on the suction side were used to locate transition. A strain gauge bridge was used to measure the root-mean-square of the bending tension to detect the buffet onset. The angle of attack was varied in the range of 0 to 8 degrees. Here, simulations at $Re_c = 3 \times 10^6$, $M_\infty = 0.70$ and $\alpha = 7.0$ deg ($\simeq 3.0$ deg above the onset) were carried out.

### 3.1. Grid and numerical setup

The unsteady computations were carried out using a PANS approach with the SST model as a RANS parent. The PANS formulation is detailed in sec. 2.2. The adoption of PANS allowed for capturing the shock oscillations. We believe that adopting reasonably high values of the parameter $f_k$ ($f_k = 0.7$ here), the PANS formulation can help in the prediction of this class of flows where most statistical turbulence models give too high levels of eddy viscosity [55,56], even working in RANS mode and for 2D simulations. Very good agreement was found between PANS and experiments for two of the aforementioned configurations [57]. On the other hand, URANS simulations with the SST model led to a steady-state solution even at angles of attack well beyond the buffet onset. The failure of the SST model to accurately predict buffet was also documented in earlier works [55,56,58].

The computational grids used for the Gurney/UTEF configurations have a typical C-H topology. A grid-sensitivity study was carried out for the uncontrolled cases [57]. For this work, we applied a local refinement to increase the resolution of the regions around the trailing edge and in the boundary layer, resulting in no modifications on the predicted frequency and amplitude of shock oscillation. The grid consists of $N_{aerofoil} = 456$, $N_{TE} = 50$ for blunt trailing edges, $N_y = 180$ in the normal direction and $N_w = 110$ in the wake.

For the spoiler configurations, the multi-block topology was slightly modified because of the hinge presence, as shown in Fig. 3. To guarantee an adequate resolution around the virtual spoiler, more grid points around the hinge and in the boundary layer were used. The numbers of cells around the aerofoil and in the normal direction now amount to $N_{aerofoil} = 756$ and $N_y = 170$, respectively. In this case, neither the presence of the hinge nor the
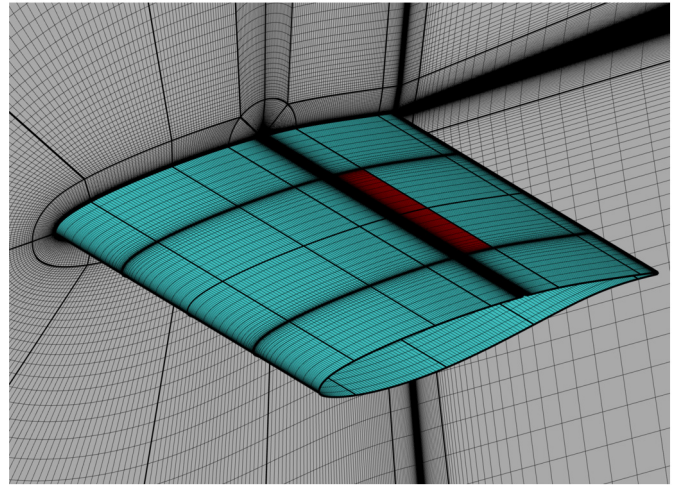


**Fig. 6.** CFD grid around the 3D OAT15A aerofoil with spoiler (red).

local grid refinement led to significant changes in the quantities associated with the shock oscillation. The spacing distribution has been set to satisfy the condition of $\Delta y^+ < 1$ at each condition, resulting in a first cell size of about $2.0 - 5.0 \times 10^{-6} c$ for the aforementioned flow conditions. Adiabatic wall boundary conditions were imposed at the aerofoil, and free-stream boundary conditions elsewhere. A timestep of $\Delta t = 0.01 c/U_\infty$ was employed, and corresponds to about 1200, 1500 and 1300 unsteady steps for the NACA0012, OAT15A and V2C sections, respectively. The convergence of the implicit scheme was based on the reduction of the flow field residual with respect to the previous step. More precisely, either a reduction of 3 orders of magnitude or 100 inner iterations of the dual-time stepping scheme must be reached for each unsteady step.

The CFD domain for the 3D computations has an extension of $L_z = c$ in the span and it is discretised using $N_z = 100$ cells in the spanwise direction. A refinement around the two spoiler ends was applied allowing for an adequate resolution of the tip vortices expected in that region. The final grid consists of about 14 million points. In this case, periodic boundary conditions were applied at the sidewalls. Fig. 6 shows the grid employed for the 3D computation, where the 2D grid, displayed on the grey plane, is the same adopted for the 2D calculations. The hinge covers the whole span and it is placed at $0.6c$ from the aerofoil leading edge. Its radius is $r_h = 0.00625c$. The spoiler is $0.08c$ long and extends for half the span.

## 4. Results

In this section, the effect of infinite and finite virtual control surfaces is investigated. In a previous publication [57], the accuracy of the PANS approach to predict buffet was established. The PANS model based on a $k - \omega$ SST model gave good results for the 2D cases and is employed in this work. First, results are shown for the three aerofoil configurations in the uncontrolled case. Then, results for infinite UTEF and spoilers, i.e. for 2D computations, are presented using both static and automatic control by means of flow reversal detection. Some aspects related to the influence of aerofoil section, angle, and length of the devices on the aerodynamic performance are also discussed. Since spoilers, unlike UTEF and Gurney flaps, are mounted on every commercial airplane, these are studied in more detail. Moreover, a combination of spoiler deployment and grid motion to simulate an aerofoil deceleration is presented to provide a simple strategy to prevent buffet from taking place when the device is retracted. Finally, a 3D computation

**Table 1**

Table of time-marching computations performed in this work.

| $M_\infty$ | $\alpha$ | Control | $L_G/c[\%]$ | $\delta_S[\deg]$ |
|---|---|---|---|---|
| **NACA0012** ($Re_c = 1 \times 10^7$) | | | | |
| 0.72 | 6.0 | - | - | - |
| 0.72 | 6.0 | Spoiler | - | 5, 10, 20 |
| | | | | |
| **V2C** ($Re_c = 3 \times 10^6$) | | | | |
| 0.70 | 7.0 | - | - | - |
| 0.70 | 7.0 | UTEF | 0.625, 2.5, 5, -5 | - |
| | | | | |
| **OAT15A** ($Re_c = 3 \times 10^6$) | | | | |
| 0.73 | 3.5 | - | - | - |
| 0.73 | 3.5 | UTEF | 0.15, 0.3, 0.6, -0.6 | - |
| 0.73 | 3.5 | Spoiler | - | 1, 2, 3, 5, 10, 15, 20 |
| 0.73 | 3.5 | Spoiler 3D | - | 5, 15 |

**Table 2**

Table of time-marching computations performed for the NACA0012 aerofoil, $Re_c = 1 \times 10^7$. Experimental results from [53].

| $M_\infty$ | $\alpha$ | Buffet | $k_{exp}$ | $k_{num}$ |
|---|---|---|---|---|
| 0.72 | 6.0 | yes | 0.55 | 0.52 |
| 0.75 | 4.0 | yes | 0.47 | 0.39 |
| 0.77 | 4.0 | yes | 0.44 | 0.45 |
| 0.80 | 4.0 | no | 0.38 | - |

**Table 3**

Table of time-marching computations performed for the OAT15A aerofoil, $Re_c = 3 \times 10^6$. Experimental results from [4].

| $M_\infty$ | $\alpha$ | Buffet | $St_{exp}$ | $St_{num}$ |
|---|---|---|---|---|
| 0.73 | 3.5 | yes | 0.066 | 0.067 |
| 0.72 | 3.5 | yes | 0.062 | 0.062 |
| 0.74 | 3.5 | yes | 0.074 | 0.071 |
| 0.73 | 3.1 | yes | 0.066 | 0.067 |
| 0.73 | 3.25 | yes | 0.066 | 0.067 |
| 0.73 | 3.9 | yes | 0.066 | 0.067 |

with finite spoiler extent is presented and the results are compared with the 2D case.

An overview of the computations carried out for this work is given in Table 1. In the table, only the simulations used to test control strategies are mentioned. Other flow conditions investigated for the uncontrolled cases for validation purposes are listed in the following section. Because of the proximity to the buffet onset for the OAT15A aerofoil, smaller UTEF lengths have been adopted.

*4.1. Uncontrolled cases*

The uncontrolled cases were first run to guarantee an accurate prediction of buffet for the test cases under analysis. For the NACA0012, four combinations of Mach number and angle of attack were investigated. They correspond to the ones investigated by McDevitt and Okuno [53] for which the reduced frequency $k_{exp} = 2\pi f_B c/U_\infty$ is available. The results are in overall good agreement with the experiments (see Table 2), although the current simulations were unable to predict buffet for the highest Mach number. This difficulty was already pointed out in the literature [55,5].

The OAT15A was investigated at $Re_c = 3 \times 10^6$. Very good agreement was found between PANS and the experiments for this aerofoil for different Mach numbers and angles of attack. The distributions of the mean pressure coefficient and the root mean square around the aerofoil were in good agreement with the experiments for several angles of attack, both at pre- and post-buffet onset (see Fig. 7, left and centre). Table 3 shows the comparison with the experiments in terms of Strouhal number associated with the main buffet frequency at different Mach numbers and angles of attack. Below $\alpha = 3.1$ deg, no SIO was detected, according to the experimental reference, while for $\alpha \geq 3.1$ deg, the amplitude of shock motion and aerodynamic coefficients (see 7, right) increases with the angle of attack. This leads to a greater smearing of the mean pressure coefficient and a higher peak in the pressure root-mean-square.

The V2C was tested at $Re_c = 3 \times 10^6$, $M_\infty = 0.70$ and $\alpha = 7.0$. This combination of angle of attack and Mach number was widely investigated during the TFAST European Project [54], where both tripped and laminar interaction were investigated. Among the numerous CFD campaign, the use of different methods led to discrepancies with the experiments. Even among the experiments,

large differences were found depending on the adopted test facility, transition location, and surface roughness. Nonetheless, at the selected flow conditions, large shock-induced oscillations are displayed, as shown in Fig. 8, and allowed us to clearly describe transonic buffet in all its phases. In general, as the angle of attack increases, the shock on a transonic aerofoil moves downstream. The shock gains intensity and leads to boundary layer separation. Two regions of flow reversal generate at the shock foot and at the aerofoil trailing edge. For a further increase of the angle of attack, the two separated flow regions merge onto a unique one, and SIO takes place. Fig. Fig. 8 shows the Mach number contours at four different instants over a period of buffet, complemented by instantaneous velocity streamlines which help visualise the local boundary layer separation. At the most downstream shock position (a), boundary layer separation takes place at the shock foot and trailing edge. Their merging onto a single, large, reversed flow region causes the local angle of attack to decrease and the shock to move upstream (b). At the most upstream position (c), the shock reaches a region of negative (favourable) pressure gradient and its intensity is reduced. Therefore, the boundary layer reattaches, and the shock starts its downstream motion (d) where both trailing edge and shock-foot separation are limited, if not absent. As the shock oscillates over a portion of the suction side, the aerodynamic coefficients undergo large oscillations, as shown in Fig. 8 (d). Most upstream and downstream shock positions coincide with minimum and maximum lift coefficient, respectively. The drag and pitching moment coefficients exhibit an analogous behaviour.

*4.2. 2D UTEF/Gurney flaps*

Results for the UTEF/Gurney configurations are here presented. For this device, the V2C and OAT15A configurations are analysed. In the first case ($Re_c = 3 \times 10^6$, $M_\infty = 0.70$ and $\alpha = 7.0$), the results show very developed buffet that exhibits a larger separation region, while in the second case ($Re_c = 3 \times 10^6$, $M_\infty = 0.73$ and $\alpha = 3.5$), the separation is less prominent. Indeed, the two configurations were analysed at angles of attack 3 and 0.5 deg higher than the respective onset angles. For the following simulations, an actuation time of $\Delta t_{act} = 0.001$, corresponding to 10 characteristic travel times, was used.
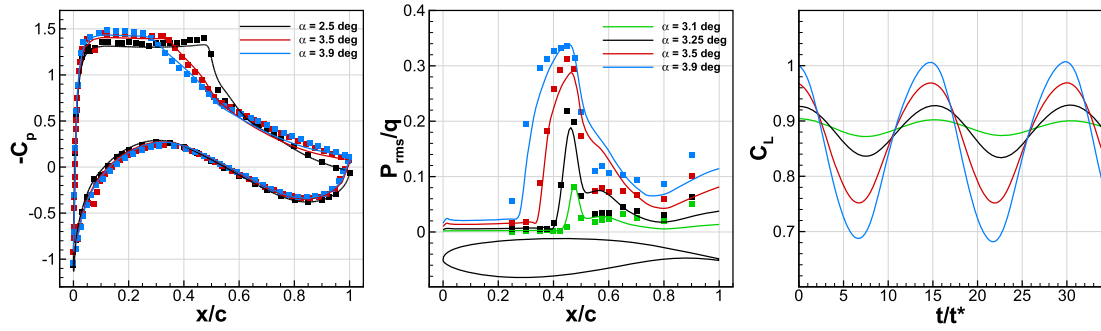
**Fig. 7.** Comparison between CFD and experiments [4] for the OAT15A aerofoil, $Re_c = 3 \times 10^6$. Left: mean pressure coefficient; centre: pressure RMS; right: lift coefficient history. Lines and symbols are coloured by angle of attack.
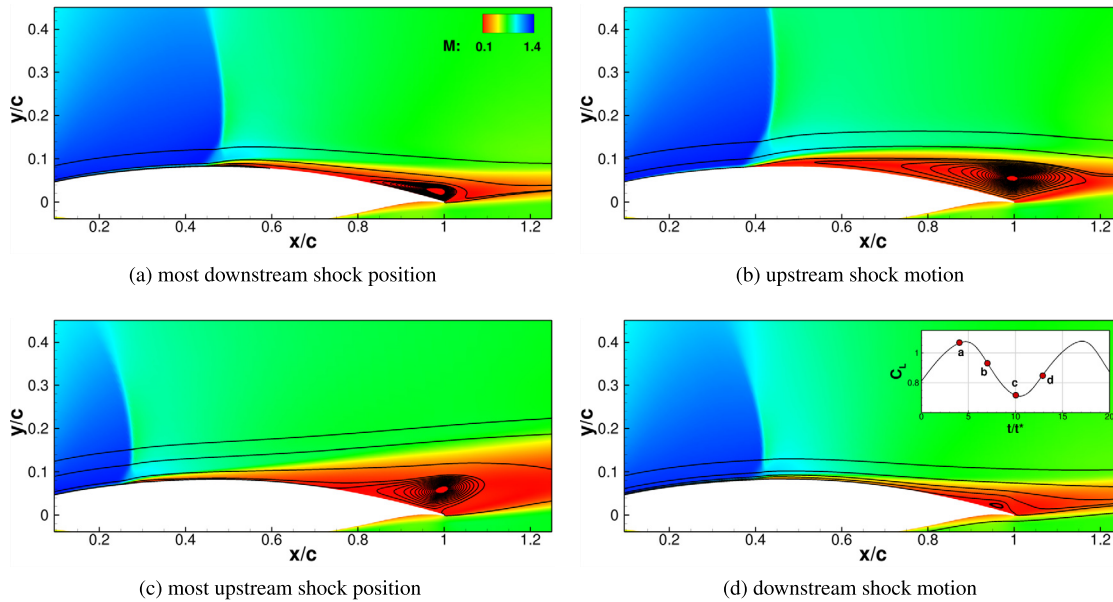


(a) most downstream shock position

(b) upstream shock motion

(c) most upstream shock position

(d) downstream shock motion

**Fig. 8.** Mach number contours and streamlines around the V2C aerofoil at $Re_c = 3 \times 10^6$, $M_\infty = 0.70$ and $\alpha = 7.0$ at selected instants over a buffet period.

*V2C section*

Trailing edge flaps were tested both as Gurney flaps and UTEF (Gurney extended on the suction side). As expected, the use of the former ones resulted in an amplification of the shock oscillation. In principle, Gurney flaps were used to enhance the performance of aerofoil for incompressible flows. Here, the deployment of Gurney flaps causes flow separation on the pressure side near the trailing edge. This results in a local increase in the angle of attack. Therefore, all the aerodynamic coefficients grew in both their mean value and amplitude of oscillation (see Fig. 9, dashed lines). The only way to stop buffet would be to deploy the flap in such a way to cross the lower buffet boundary (also known as *buffet offset* [55]) and induce stall. Nevertheless, since cruise flight conditions are below the upper buffet boundary (*buffet onset*), it is advisable to suppress the SIO by a reduction of either angle of attack or Mach number. Therefore, the aforementioned strategy is discouraged.

Given the inadequacy of Gurney flaps for this problem, the UTEF configuration was studied. For this configuration, three UTEF lengths were tested: $L_{UTEF}/c = 0.00625$, 0.025, and 0.05. Fig. 9 shows a progressive decrease in the amplitude of oscillation of the aerodynamic coefficient as the UTEF length increases for $L_{UTEF}/c > 0.00625$. While a short device ($L_{UTEF}/c = 0.025c$) only contributes by alleviating buffet, a longer one ($L_{UTEF}/c = 0.05c$) is able to suppress the oscillation. Fig. 10 shows the longitudinal velocity contour around the aerofoil with longest UTEF at steady-state. Con-

trarily to the UTEF case, the separation region generated near the trailing edge on the suction side results in a local angle of attack decrease. As a consequence, the shock is pushed upstream and the separation region is split into two different ones, one at the shock foot and another at the trailing edge. The aerofoil curvature and angle of attack are such to result in a strong flow acceleration ($U_{max}/U_\infty \simeq 1.7$). The resulting shock, even if weakened by the effect of the UTEF, is strong enough to separate the boundary layer underneath. Since the shock is now in the first half of the aerofoil, i.e. in a region of favourable pressure gradient, the boundary layer reattaches almost immediately and the separated region does not merge with the one at the trailing edge. The detailed view of the aerofoil trailing edge (Fig. 10, right image) shows the streamlines around the UTEF. The flow stagnates and recirculation takes place in front of the UTEF. This figure shows the ability of the method of imposing no slip conditions on the infinitely thin device and capturing the vortices that detach behind the flap.

The steady-state values of the aerodynamic coefficients are approximately equal to the mean at buffet conditions. This device did not introduce penalties in terms of drag nor a lift/moment increase.

*OAT15A section*

The same study was repeated for the OAT15A aerofoil. As the angle of attack is only 0.4 deg above the predicted buffet onset, shorter UTEF heights were used with respect to the previous case. Similar considerations hold for both the Gurney and UTEF con-
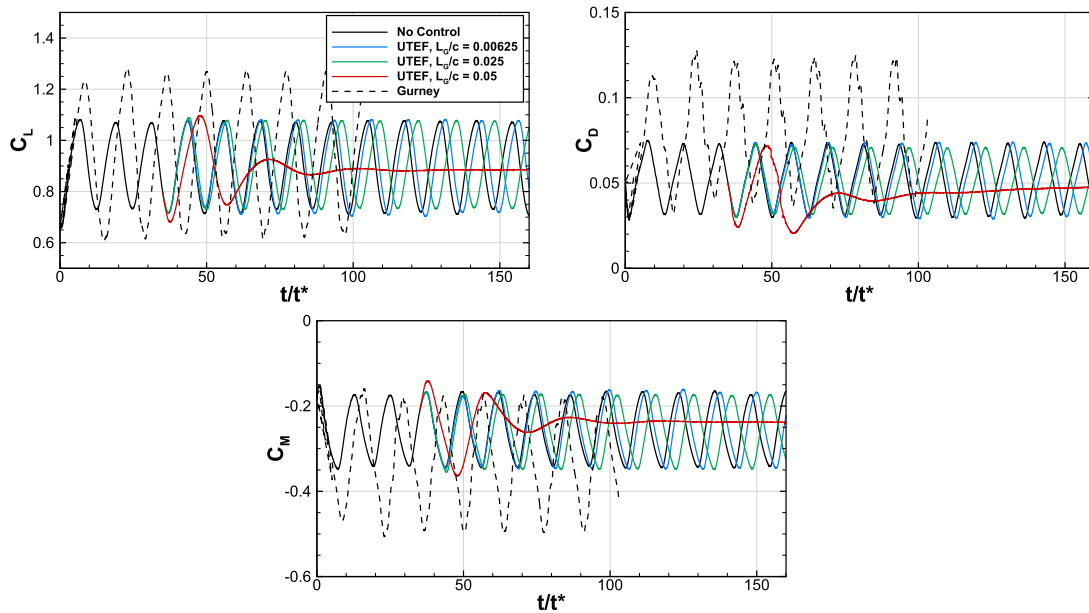
**Fig. 9.** Aerodynamic coefficients for the V2C aerofoil at $Re_c = 3 \times 10^6$, $M_\infty = 0.70$ and $\alpha = 7.0$, for different lengths of the Gurney/UTEF.
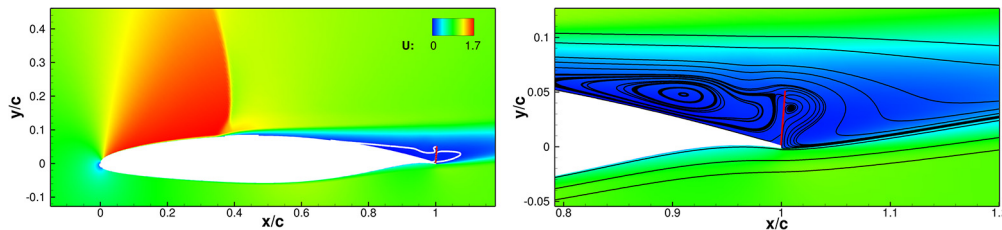


**Fig. 10.** Longitudinal velocity contour around the V2C aerofoil at $Re_c = 3 \times 10^6$, $M_\infty = 0.70$ and $\alpha = 7.0$, with UTEF. The solid, white line indicates the $U/U_\infty = -0.001$ isoline.

figurations. A main difference is the values of the aerodynamic coefficients with respect to the mean values at buffet conditions. Indeed, an increase in the amplitude of the aerodynamic coefficients is visible in Fig. 11. The main reason is that the upstream shock position no longer induces boundary layer separation at the shock foot (see Fig. 12), while in the previous case, prominent separation was still present.

For the UTEF configuration, even a 0.15% $c$ long device was able to suppress the SIO. Given the proximity to the buffet onset ($\alpha - \alpha_{\text{onset}} = 0.4$ deg), a smaller effort is required to alleviate buffet.

### 4.3. 2D spoilers

#### 4.3.1. Open loop control

This section presents the results for an open loop control by means of spoilers. The NACA0012 and OAT15A were analysed at buffet conditions. The first configuration was studied under buffet conditions with prominent separation on the aerofoil suction side. The OAT15A was investigated at the same flow conditions of section 4.2. Moreover, for the latter case a sensitivity study to the spoiler angle was carried out. Differences between the configurations are pointed out.

#### NACA0012 section

At buffet conditions around the NACA0012 aerofoil, the spoiler deployment angles amount to 10 and 20 deg. When the spoiler is not deployed, $\delta_s = 0$ deg in Fig. 13, the effect of the hinge slightly dampens the oscillations as can be seen from the aerodynamic coefficients histories in Fig. 13. When the spoiler is deployed, the oscillations are suppressed, with a transient time that shortens

with the amplitude of $\delta_s$. Fig. 14 shows the effect of the spoiler on the separated region by means of longitudinal velocity contours and streamlines. The separation region is perturbed in the low angle-case while it is broken into two parts in the high angle-case, resulting in a stabilization of the shock position. This situation is particular because the separation is prominent even for the baseline flow. Therefore, the size of the separated region does not vary significantly when the spoiler is added, and the spoiler only contributes by avoiding the propagation of disturbances in the boundary layer. For smaller $\delta_s$, the separated flow region is not completely broken and the transient is longer. For this case, the values of the aerodynamic coefficients at steady-state do not differ significantly from the average one in baseline case, as for the V2C in section 4.2.

#### OAT15A section

For the OAT15A case, the history of the aerodynamic coefficients in response to an instantaneous deployment of the spoiler at different angles $\delta_s$ is shown in Fig. 15. In Table 4, the contribution of the spoiler is distinguished from the part of the loads that does not account for the additional surface. Also, the viscous and pressure contributions on the drag are distinguished in Table 4. The steady-state values of the four coefficients are collected in Table 4 and Fig. 18. The lift coefficient $C_L$ tends towards a steady-state value even for a small deflection of the spoiler (see Fig. 15 (a)). Unlike for the NACA0012 case, a small deflection of the spoiler allows for the buffet to be canceled. The lift increase is not due to the presence of the spoiler itself, but to the ability of the device to stabilize the shock at a position that is downstream of the mean position during the buffet motion. The main drawback with
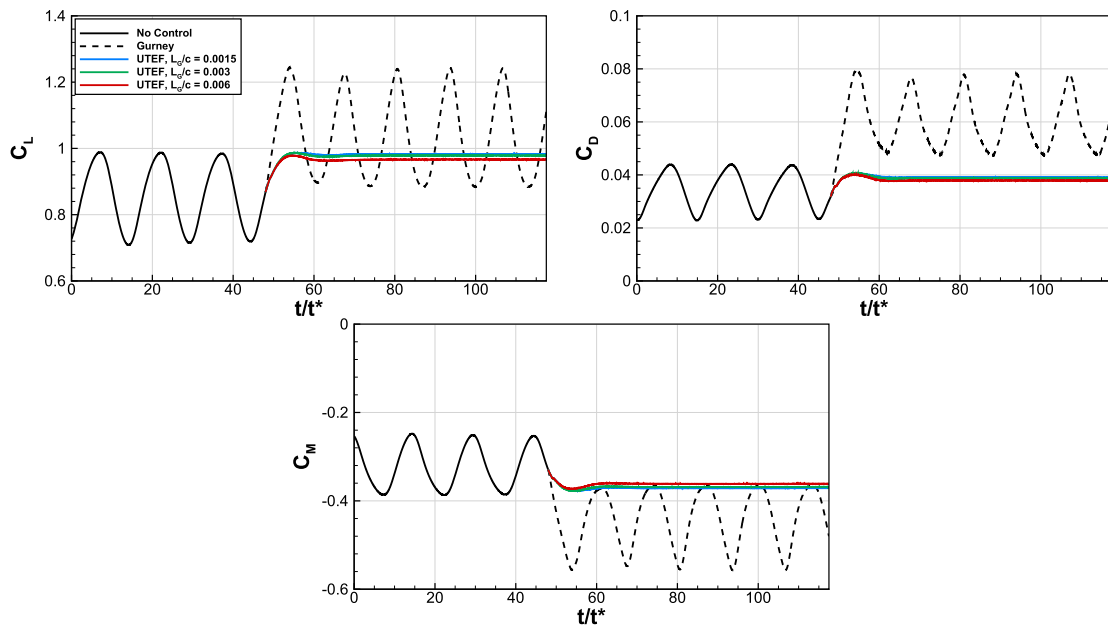
**Fig. 11.** Aerodynamic coefficients for the OAT15A aerofoil at $Re_c = 3 \times 10^6$, $M_\infty = 0.73$ and $\alpha = 3.5$, for different lengths of the Gurney/UTEF.
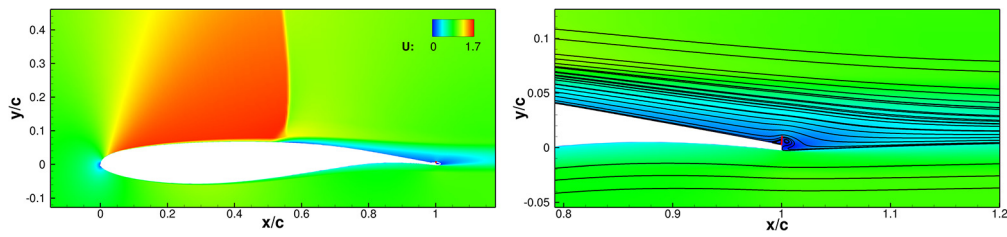


**Fig. 12.** Longitudinal velocity contour around the OAT15A aerofoil at $Re_c = 3 \times 10^6$, $M_\infty = 0.73$ and $\alpha = 3.5$, with UTEF. The solid, white line indicates the $U/U_\infty = -0.001$ isoline.
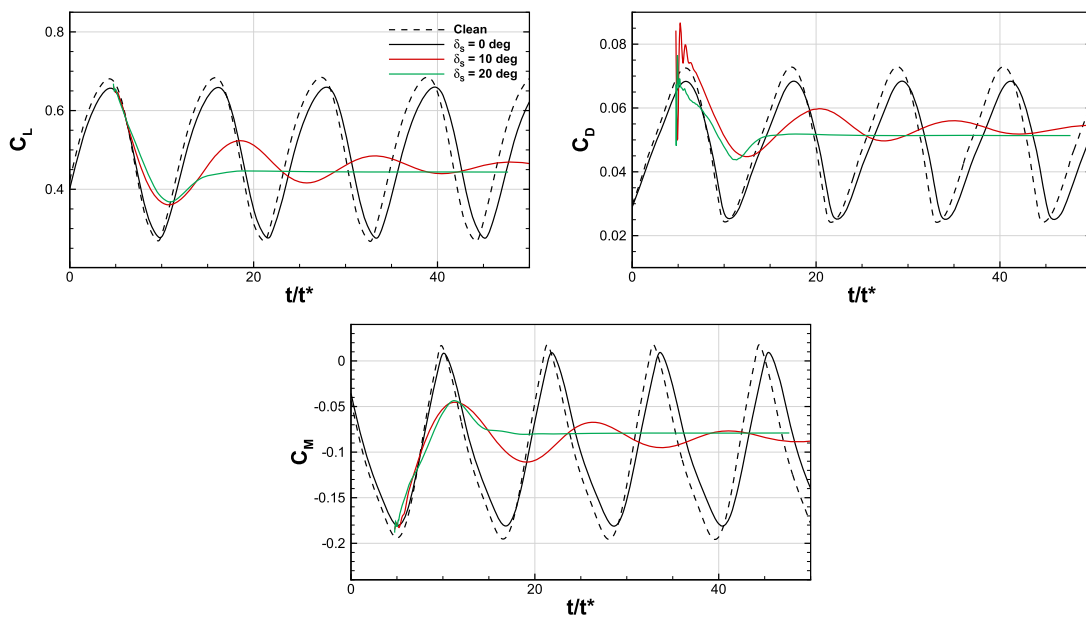


**Fig. 13.** Aerodynamic coefficients history for different angles of spoiler deployment $\delta$ on the NACA0012 at $Re_c = 10 \times 10^6$, $M_\infty = 0.72$ and $\alpha = 6.0$.

(a) $\delta_S = 10$ deg

(b) $\delta_S = 20$ deg
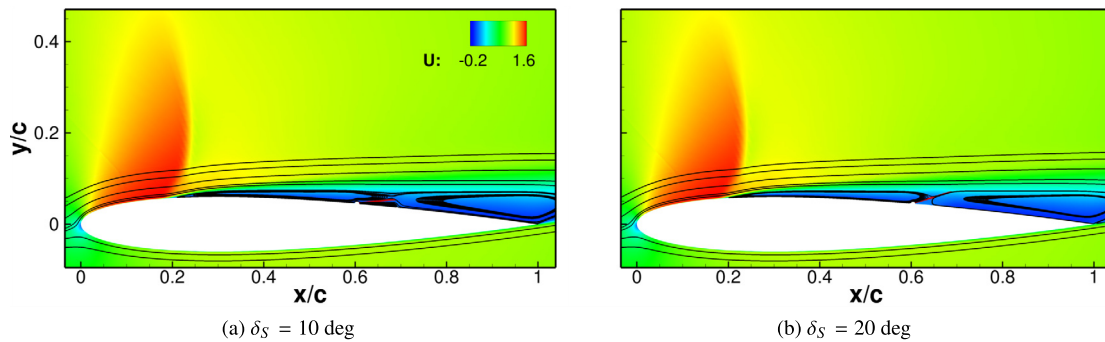
**Fig. 14.** Streamwise velocity component contours for different angles of spoiler deployment $\delta$ on the NACA0012 at $Re_c = 10 \times 10^6$, $M_\infty = 0.72$ and $\alpha = 6.0$.
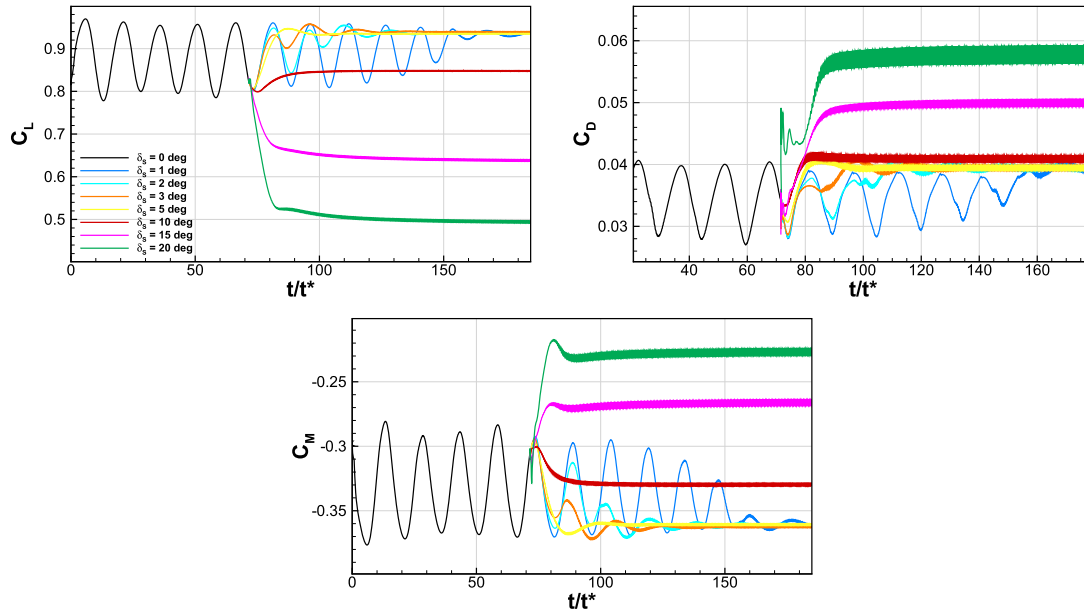


**Fig. 15.** Histories of aerodynamic coefficients for different angles of spoiler deployment $\delta$ on the OAT15A aerofoil at $Re_c = 3 \times 10^6$, $M_\infty = 0.73$ and $\alpha = 3.5$ deg.

respect to the previous geometry is the increase in the drag coefficient $C_D$ (see Fig. 15 (b)). The main difference is that in the previous case of prominent separation, the spoiler was immersed in the separated flow region and no significant pressure difference was present between the two faces. In this case, a net pressure jump is visible across the spoiler hinge, as shown in Fig. 16, left plot. The pressure jump has a local minimum for $\delta_s = 5$ deg, and increases significantly at higher angles. In this situation, the spoiler no longer represents a shock control device and behaves as an air-breaker. Under such conditions, the drag significantly increases with respect to the uncontrolled case value.

The right panel of Fig. 16 shows the pressure distribution comparison between the controlled case at $\alpha = 3.5$ deg and the uncontrolled case at both pre- and post-buffet onset. For the uncontrolled buffet case, the mean pressure coefficient distribution is smeared because of the shock oscillation on the suction side. In the other two cases, the pressure jump corresponding to the shock can be easily detected. The presence of the spoiler creates a separated flow region where the pressure is lowered. As a result, the shock intensity required to obtain a smaller pressure jump leads to a more upstream position of the shock itself. As a consequence of the modified load distribution the pitching moment $C_m$ increases (see Fig. 15 (c)). At small $\delta_S$, the shock position is fixed at a downstream position with respect to the mean shock position for the uncontrolled case. Therefore, the lift distribution is higher in the first half of the airfoil, while it is almost unchanged in the sec-

ond part. This results in a mild nose-up effect. On the other hand, higher spoiler deflection angles correspond to an upstream shock position and reduced pressure after the hinge on the suction side. In these cases ($\delta_S > 10$ deg), the lift distribution along the chord with respect to the uncontrolled case is sensibly smaller before the hinge and higher after the hinge. As a consequence, the aerofoil undergoes a nose-down effect.

To better understand the spoiler effect at different angles, velocity contours complemented with streamlines are shown in Fig. 17, top panels, for a spoiler deflection angle of $\delta_s = 5$, 10, and 20. The separated flow region behind the spoiler acts by reducing the angle of attack and pushing the shock close to the leading edge where it loses strength. This effect is more evident as $\delta_s$ increases. For $\delta_s = 5$ deg and $\delta_s = 10$ deg, the shock is strong enough to separate the boundary layer and the spoiler breaks the communication between the two recirculation regions. In the other case, the shock is pushed further upstream and the boundary layer is attached upstream of the spoiler. This is particularly interesting because not only the spoiler acts to stabilise the shock in response to a trailing edge action, like in the UTEF case, but it proves useful by interfering with the communication in the separated region with its presence. The presence of the spoiler for $\delta_s \leq 10$ prevent the merging of the two separated flow regions into a fully separated boundary layer (see Fig. 17, bottom panels), which is a necessary condition for buffet.
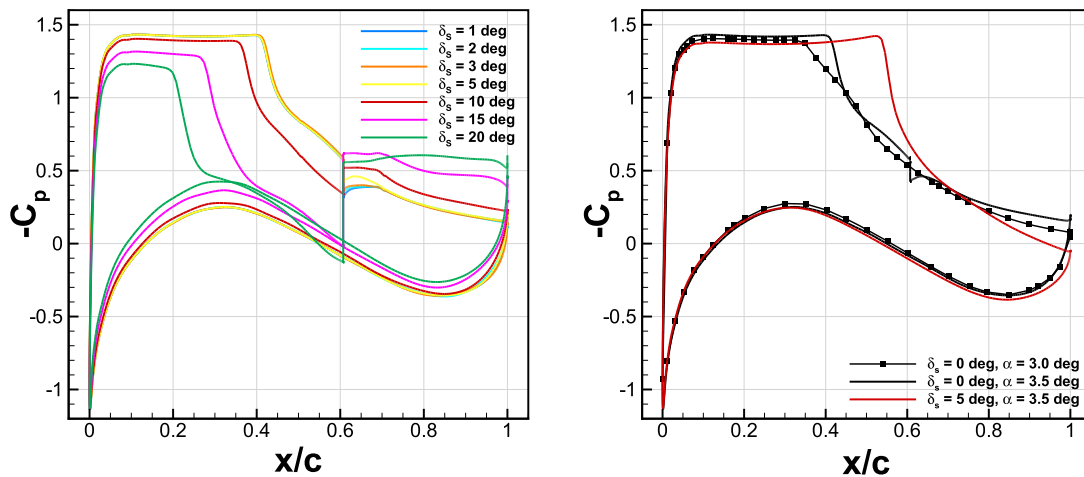
**Fig. 16.** Pressure coefficient distribution for different angles of spoiler deployment $\delta_S$ around the OAT15A aerofoil, $Re_c = 3 \times 10^6$, $M_\infty = 0.73$ and $\alpha = 3.5$.
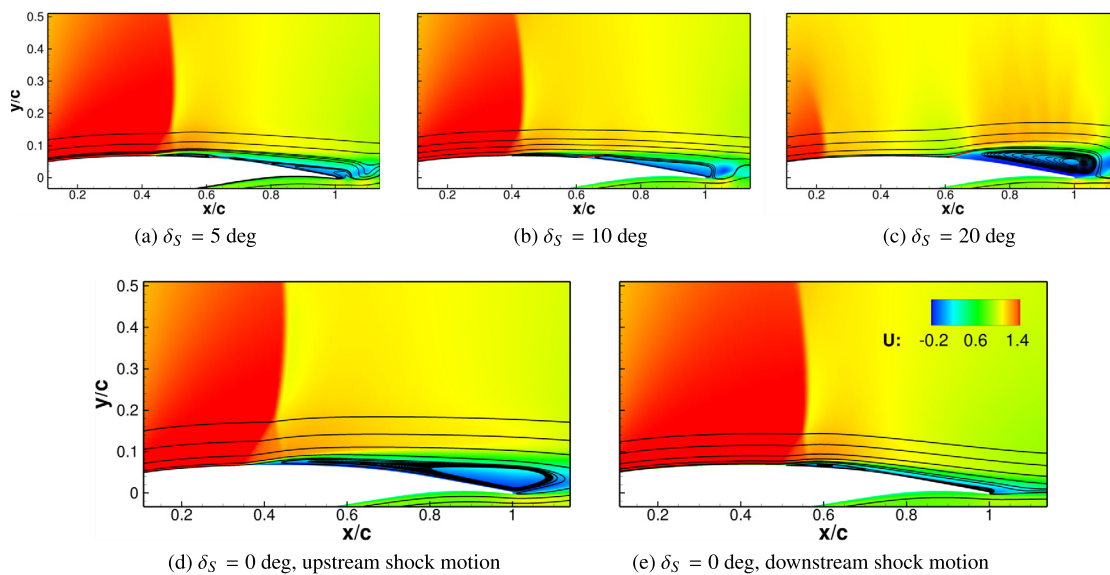


(a) $\delta_S = 5$ deg

(b) $\delta_S = 10$ deg

(c) $\delta_S = 20$ deg

(d) $\delta_S = 0$ deg, upstream shock motion

(e) $\delta_S = 0$ deg, downstream shock motion

**Fig. 17.** Top: streamwise velocity component contours for different angles of spoiler deployment $\delta_S$ on the OAT15A aerofoil at $Re_c = 3 \times 10^6$, $M_\infty = 0.73$ and $\alpha = 3.5$; bottom: same visualisation during upstream and downstream shock motion.

Table 4 and Fig. 18 sum up the effect of $\delta_s$ on the aerofoil aerodynamic performance. Even a small deflection of the spoiler ($\delta_s = 1$ deg was the smallest value) resulted in buffet suppression. For a small spoiler deflection $\delta_s = 1 - 5$ deg, the lift increased with respect to the mean one at buffet conditions, and the smallest drag penalty was introduced together with an additional nose-up contribution. At higher $\delta_s$, the lift decreased and the drag penalty was even higher. Due to the modified pressure distribution in "air-breaker mode", the aerofoil undergoes a nose-down effect. Fig. 18 (d) shows the activation-to-steady-state time $t_{ss}$. Due to the reduced $t_{ss}$ with respect to the other angles, $\delta_s = 5$ deg was chosen to be the optimal one. Although a short response time is not optimal for applications, it is surely convenient for reducing CFD costs associated with an higher response times (as in the case of $\delta_s = 1$).

It is worth noting that the aerodynamic coefficients exhibit increasingly wider oscillations as $\delta_s$ increases. The reason resides in the vortex shedding occurring behind the aerofoil as the size of the separated flow region changes. Regardless of the spoiler angle, the flow separates behind the spoiler up to the trailing edge and the thickness of the separated region increases with $\delta_s$ (see Fig. 19). The separated flow region acts as a thickened trailing edge, and vortex shedding with increasing vortex size takes place. Larger vor-

tices results in wider fluctuations in the aerodynamic coefficients, as shown by the correlation between Fig. 19 and Fig. 15.

### 4.3.2. Automatic spoiler deployment

Here it is shown how the spoiler is activated when flow separation is detected by a probe placed on the aerofoil surface at $x/c = 0.7$. The effect of the deployment duration $T_{on}$ on the aerodynamic loads was previously studied. $T_{on}$ is evaluated as $T_{on} = dt \, \Delta t_{act}$. Longer $T_{on}$ resulted in a slower suppression of buffet. For practical applications, considered the short buffet period (the buffet frequency for the OAT15A case is $f_B = 69$ Hz), a relatively long actuation time is recommended. It allows avoiding too sudden changes in the aerodynamic loads that could create passenger discomfort. From the CFD point of view, a slower deployment of the control surface is advisable as drastic changes in the flow field can be avoided. In our case, the full deployment in over 1000 unsteady steps was considered a compromise between accuracy and efficiency.

Fig. 20 shows the drag coefficient (top) and local longitudinal velocity (bottom) for the simulation around the NACA0012 aerofoil for a $\delta_{max}$ of 5 deg. Because of its rapid increase at the activation, $C_D$ clearly shows the control activation. In this case, the control

**Table 4**

Steady-state aerodynamic coefficient for different spoiler deflection angles for the OAT15A aerofoil, $Re_c = 3 \times 10^6$, $M_\infty = 0.73$ and $\alpha = 3.5$ deg. $C_L$: lift coefficient; $C_D$: drag coefficient; $C_m$: pitching moment coefficient; $t_{ss}$ activation-to-steady-state time; $v$-subscript: viscous component; $p$-subscript: pressure component; $s$-subscript: spoiler contribution. The $\overline{(\cdot)}$ indicates that these are averages takes over several periods of the residual oscillations in the flow.

| $\delta_s$ [deg] | $\overline{C_L}$ | $\overline{C_{L_s}}$ | $\overline{C_{D,p}}$ | $\overline{C_{D,p_s}}$ | $\overline{C_{D,v}}$ | $\overline{C_{D,v_s}}$ | $\overline{C_m}$ | $\overline{C_{m_s}}$ | $t_{ss}/t^*$ |
|---|---|---|---|---|---|---|---|---|---|
| 0 | 0.867 | | 0.0346 | | 0.00375 | | -0.327 | | |
| 1 | 0.927 | 0.0085 | 0.0398 | 0.0011 | 0.00411 | 0.00035 | -0.359 | -0.00061 | $\simeq 150$ |
| 2 | 0.929 | 0.0079 | 0.0392 | 0.0009 | 0.00399 | 0.00022 | -0.361 | -0.00058 | $\simeq 90$ |
| 3 | 0.933 | 0.0072 | 0.0396 | 0.0007 | 0.00392 | 0.00015 | -0.363 | -0.00053 | $\simeq 85$ |
| 5 | 0.927 | 0.0019 | 0.0396 | 0.0001 | 0.00379 | 0.00005 | -0.362 | -0.00036 | $\simeq 50$ |
| 10 | 0.838 | -0.0146 | 0.0404 | 0.0004 | 0.00346 | -0.00006 | -0.331 | 0.00016 | $\simeq 45$ |
| 15 | 0.625 | -0.0374 | 0.0494 | 0.0045 | 0.00353 | -0.00009 | -0.265 | 0.00094 | $\simeq 110$ |
| 20 | 0.485 | -0.0416 | 0.0570 | 0.0082 | 0.00368 | -0.00006 | -0.224 | 0.00134 | $\simeq 110$ |
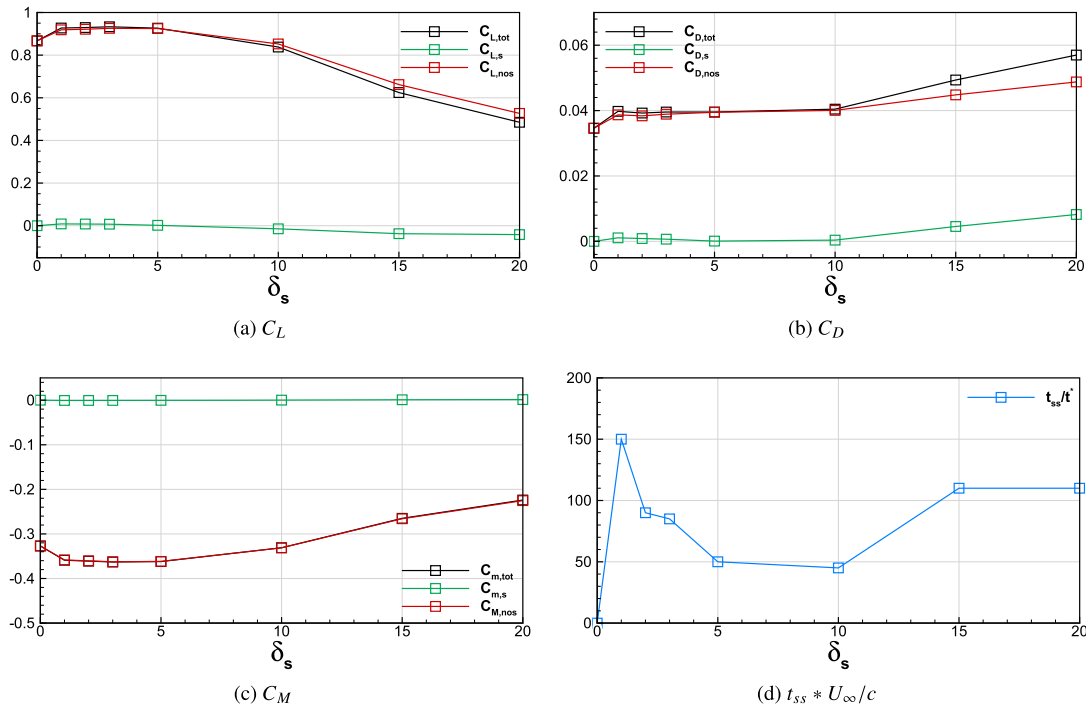


**Fig. 18.** Steady-state values of the aerodynamic coefficients for different angles of spoiler deployment $\delta_s$ around the OAT15A aerofoil, $Re_c = 3 \times 10^6$, $M_\infty = 0.73$ and $\alpha = 3.5$. The spoiler (*s* subscript) is distinguished from the one with no spoiler (*nos* subscript).

routine started at $t/t^* = 20$, and flow reversal was detected at $t/t^* \simeq 23$. After the drastic increase in drag, the oscillations are alleviated. As shown in Fig. 14, after the spoiler deflection, the region behind the spoiler is fully separated and this is confirmed by the negative velocity in Fig. 20, bottom plot.

*4.3.3. Spoiler retraction and aerofoil deceleration*

The second part of the actuation is here discussed. As mentioned in section 2.3.4, the spoiler must be retracted after the oscillations are suppressed. As underlined in the previous sections, the deployment of the spoiler results in a variation of the aerodynamic coefficients. For instance, a sudden increase in the drag coefficient should result in the aerofoil deceleration and the addition of a local velocity component (positive if the free-stream is aligned with the positive x-axis). In turn, the load distribution changes. If not by moving the CFD grid, this effect should be taken into account by modifying Mach number and angle of attack (if the aerofoil undergoes changes in the moment coefficient).

Changes in the aerodynamic loads are usually not accounted for in CFD simulations. As a result, once the spoiler is retracted, the oscillation occurs again and cancels the effect of the flow control. An example is given in Fig. 21. It shows the history of the aerodynamic loads during and after the spoiler deployment. When the spoiler is retracted within the aerofoil (blue and red lines in

figure), the coefficients come back to the pre-actuation oscillating behaviour.

Here, the aerofoil deceleration is simulated by moving the CFD grid in the direction of the free-stream, as explained in section 2.3.4. The motion was prescribed along the free-stream direction to only represent the drag variation, deemed as preponderant over lift and moment in the previous section. The CFD grid acceleration, velocity and position follow eq. (6), where the initial and final Mach number are 0.73 and 0.71, respectively. The method is effective in preventing buffet from taking place again, as indicated by the black line in Fig. 21. For the sake of clarity, the steady-state values of the aerodynamic coefficients at $M_\infty = 0.71$ were added. These latter were rescaled by a factor $(0.71/0.73)^2$ to account for the difference in reference Mach number with respect to the other simulations (solid lines).

However, some aspects must be discussed. The one degree-of-freedom assumption made for this case is only a crude approximation to describe a possible deceleration due to a pilot action or an increase in drag caused by the spoiler deployment. In reality, the dynamic response to the spoiler deployment would generate a disequilibrium in lift, drag, and pitching moment (see, e.g., Fig. 15), significantly complicating the treatment of this problem. Therefore, the use of a spoiler alone cannot be defined as successful unless the dynamic response of the airfoil is studied. This consideration
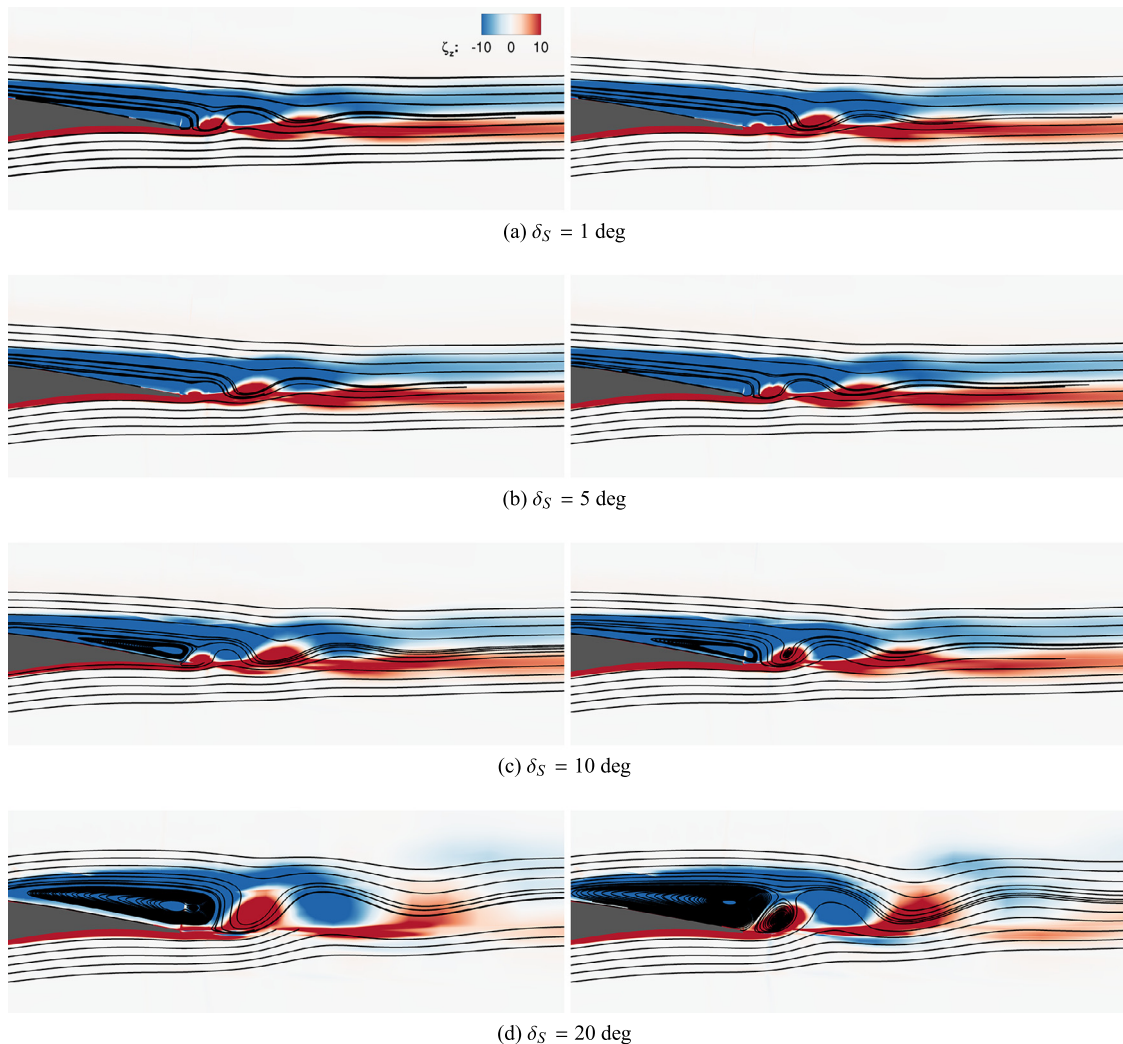
(a) $\delta_S = 1$ deg

(b) $\delta_S = 5$ deg

(c) $\delta_S = 10$ deg

(d) $\delta_S = 20$ deg

**Fig. 19.** Z-vorticity contour and streamlines around the TE of OAT15A aerofoil at $Re_c = 3 \times 10^6$, $M_\infty = 0.73$ and $\alpha = 3.5$ deg. From top to bottom: $\delta_S = 1, 5, 10, 20$ deg. Left and right snapshots are taken at different instants over a period of the oscillations highlighted in Fig. 15.

holds for any other dynamic control strategy. In principle, buffeting flows see strong oscillations in the aerodynamic coefficients and their study should account for the dynamic response of the structure. So far, this practice has not been adopted, with the exception of Scharnowski et al. [59] who left their experimental model free to pitch. Here, the applied deceleration can be seen as a first step towards this kind of approach to simulate a response to the spoiler deployment. On the other hand, the imposed deceleration can be interpreted as an action of the pilot to escape the buffet boundary. In particular, the spoiler deployment temporarily suppresses buffet, and the deceleration allows moving towards conditions where SIO is not present. The shock stabilisation is desired to avoid a possible, temporary increase in the oscillation amplitude due to the aerofoil deceleration. Therefore, spoilers (and UTEF) thought as a temporary solution for buffet alleviation, do not extend the buffet boundary. When needed, they can be deployed to suppress the shock-induced oscillations, allowing the pilot to return to conditions below the buffet boundary. If the effect of these devices is considered as a simple shape modification, it can be said that spoilers and UTEF delay the onset of buffet (see the works of Tian et al. [37,17]).

### 4.4. 3D control

This section presents results for the finite spoiler case applied on the OAT15A wing. The investigated angles of attack are $\delta_s =$

5 and 15 deg. The first is optimum for the 2D case when it comes to lift increase and time of actuation, while the second corresponds to an off-design actuation.

Fig. 22 shows the influence of flow control on the aerodynamic coefficients. In every case, the SIO is suppressed within some buffet periods. With respect to the 2D counterpart, the 3D case at $\delta_s = 5$ deg is affected by the limited spanwise extent of the flow control device and the response time is increased. The same holds for the effect the spoiler has on the steady-state value of the aerodynamic coefficient. This is extremely positive when one looks at the drag coefficient, as it drops significantly with respect to the 2D case. For the case $\delta_s = 5$, the steady-state values of moment and lift coefficients now roughly coincide with their mean values at buffet conditions. The delay in the time response is not significant: given the frequency of buffet, a response time of 3 to 5 buffet periods corresponds to less then 0.1 s, which is more than satisfactory for every practical application. The $\delta_s = 15$ case presents a different behaviour, in agreement with the 2D results of section 4.3.1. Lift and moment coefficients have similar values to the 2D computation, while the drag is drastically reduced. In both cases, small oscillations in the aerodynamic coefficients remain (see the zoomed view in Fig. 22, top-right). The causes were explored in section 4.3.1 and the same considerations hold for the 3D cases. As the vortex shedding shown in Fig. 19 now only occurs on roughly half of the spanwise extent of the domain, the
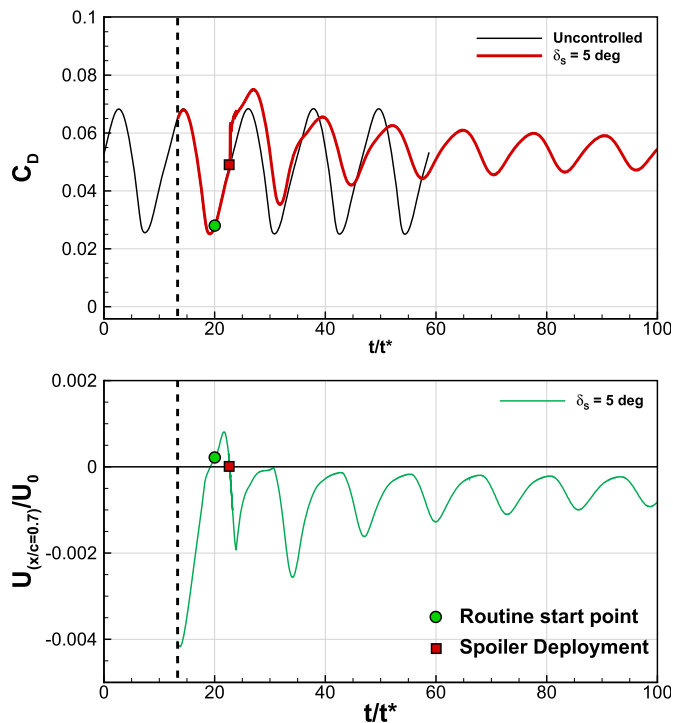
**Fig. 20.** Aerodynamic coefficients history in response to an automatic spoiler deployment on the NACA0012 aerofoil at $Re_c = 10 \times 10^6$, $M_\infty = 0.72$ and $\alpha = 6.0$.

influence on the aerodynamic coefficients is milder with respect to the 2D cases.

The steady-state pressure distribution in Fig. 23, top figures, shows a curved shock front at both angles. In agreement with the 2D cases, the shock is pushed upstream with respect to its pre-onset position. This effect is more significant at the spanwise positions seeing the presence of the spoiler, while the shock position is more downstream elsewhere. In the $\delta_s = 15$ deg case, the flow is compressed between the shock and the spoiler, accentuating the pressure jump across the hinge. The high $\delta_s$ case sees a stronger 3D effect, since the pressure distribution differs significantly according to the spanwise section considered. The lower pressure jump across the hinge with respect to the 2D case justifies the drop in drag observed in Fig. 22.

Friction lines in Fig. 24 complement the results of Fig. 23 and corroborate those of the 2D computations. In the same plot, $M_\infty = 1$ Mach surfaces show the shock position, $U/U_0 = -0.001$ iso-surfaces indicate the extent of the separated regions, and friction lines help visualize the spanwise flow organization. In the $\delta_s = 5$ case, the rear shock position results in a separated flow region spanning from the shock foot to the spoiler, while for a higher spoiler angle, an aft shock position allows the boundary layer to re-attach. In the latter, the flow decelerates before turning around the spoiler resulting in a higher pressure jump across the control surface and drag penalty. The results are in line with the 2D cases. The main difference consists of the flow structure out of the portion covered by the spoiler, where the flow re-attaches. Therefore, the effect of the finite control surface is mitigated.

The pressure difference between the upper and lower surface of the spoiler results in two counter-rotating tip vortices which are well captured in the computations. The higher the $\delta_s$, the more intense the vortices, as shown in Fig. 25. Overall, the spanwise finite spoiler gives rise to two systems of vortices: the spanwise vortices detaching as a result of the trailing edge thickening, typical of the 2D case, and the longitudinal tip vortices. The deployment of the spoiler leads to the suppression of buffet by fixing flow separation on a portion of the wing.

## 5. Conclusions and future work

In this work, numerical simulations of virtual spoilers, upper trailing edge flaps, and Gurney flaps were carried out in the context of transonic buffet control. A PANS model based on a k-$\omega$ SST model was used to simulate the flow around two- and three-dimensional configurations, providing accurate results for the prediction of the SIO. Control devices were approximated by means of no-slip, infinitely thin surfaces. The adoption of the method used in this work allowed for an easy study of the same flow with different geometric properties of spoilers and flaps, such as angle of deployment and/or length of the devices. Even with the adoption of virtual surfaces, the simulations captured well flow separation and/or vortices in 2D and 3D computations.

Gurney flaps and UTEF were tested for two two-dimensional configurations: the V2C and OAT15A aerofoils. The separation region generated on the pressure side by the Gurney flaps resulted in an increase of the local angle of attack. Therefore, Gurney flaps did not alleviate buffet. Conversely, they caused an increase in the shock oscillation amplitude, as well as in the fluctuations of the aerodynamic coefficients.

The deployment of the Gurney on the suction side was able to alleviate, if not to suppress, the shock oscillations around the airfoils. The separated flow region at the trailing edge generated by these devices resulted in an upstream shock position. The shock weakened and the separation could be avoided. For both configurations, the SIO was suppressed only when the shock was pushed upstream enough to prevent the merging of the two separated flow regions at the shock foot and at the trailing edge. For the V2C aerofoil, studied under very developed buffet conditions, a small device did not produce the desired effect, and a longer one was needed.

On the other hand, spoilers proved able to stop the buffet by hampering the communication between the shock-foot and the trailing edge separation regions. Two airfoils were investigated in the 2D campaign: the NACA0012 and the OAT15A aerofoils. In the first case, because of the flow conditions and the airfoil geometry, the separated flow region in the buffet case was much larger. Therefore, a greater spoiler deployment was necessary to suppress buffet. Nevertheless, even a small spoiler angle alleviated the oscillations. For the OAT15A aerofoil, even a small deployment of the spoiler revealed effective in reducing the SIO. If the spoiler is deployed enough, the shock position is such to avoid boundary layer separation, otherwise two distinct regions remain and the spoiler prevents their interaction. Unlike the UTEF, spoilers proved to be able to suppress the oscillations even when the boundary layer is fully separated after the shock since the separated flow region is broken by the presence of the device. For small spoiler deployment angles, the control surface functions as an obstacle for disturbances travelling in the boundary layer.

On the OAT15A, 3D simulations were repeated adopting a finite spoiler at two deployment angles. The limited span of the control surface resulted in a mitigation of its effect compared to the 2D case. While the differences in the lift and pitching moment were negligible between the 2D and 3D cases, the drag penalty significantly reduced in the 3D configurations. At a higher deployment angle, the separation behind the spoiler is more severe, and the device acts as an air-breaker.

The use of flow control was also complemented with an aerofoil deceleration to simulate the effect of the pilot action to escape the buffet regime. While the spoiler was able to suppress the oscillations, the deceleration applied by means of CFD grid motion resulted in a local Mach number decrease and a successful prevention of buffet. The test performed here did not account for the dynamic response of the aerofoil to the spoiler deployment.
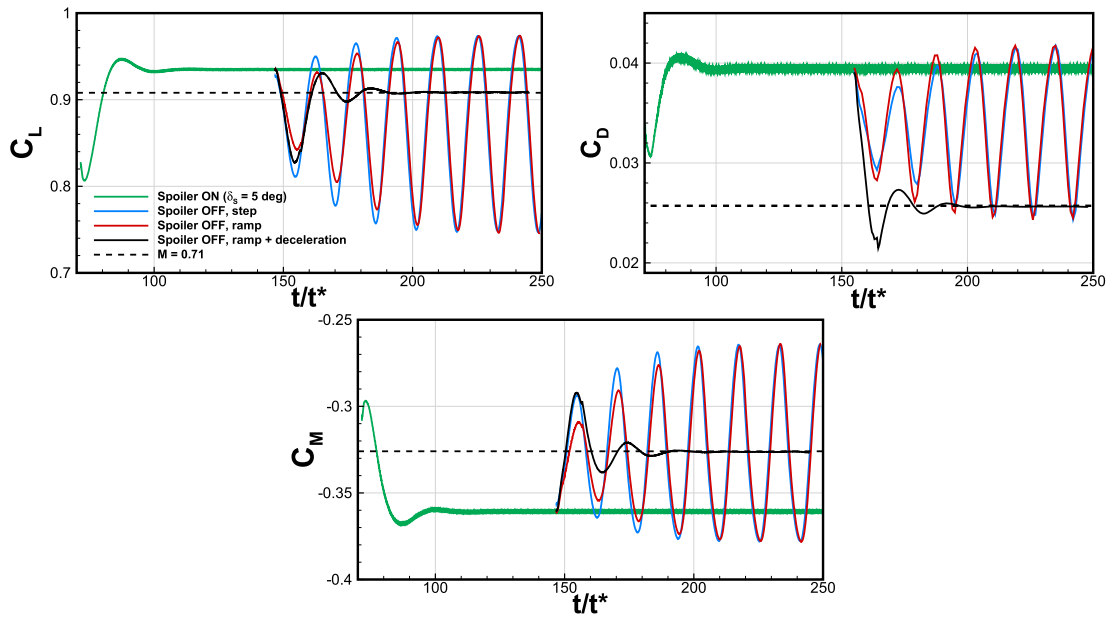
**Fig. 21.** Aerodynamic coefficients history for 2D simulations on the OAT15A wing section at $Re_c = 3 \times 10^6$, $M_\infty = 0.73$ and $\alpha = 3.5$ deg in response to the spoiler retraction. The dashed lines represent the steady-state values of the aerodynamic coefficients at $Re_c = 3 \times 10^6$, $M_\infty = 0.71$ and $\alpha = 3.5$ deg.
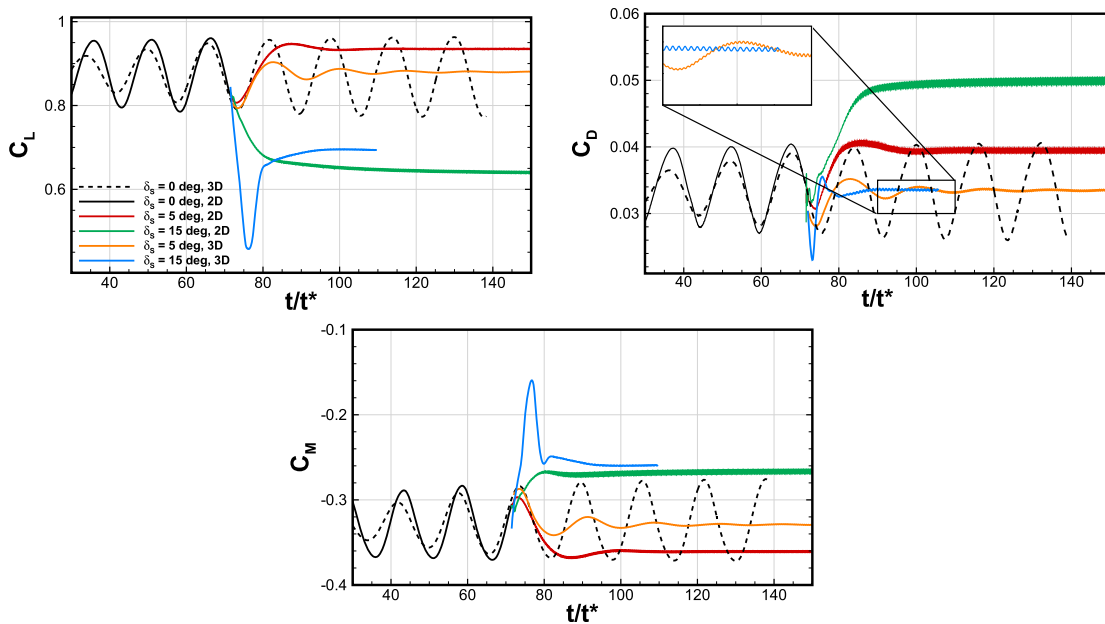


**Fig. 22.** Aerodynamic coefficients history for 2D and 3D simulations on the OAT15A wing section at $Re_c = 3 \times 10^6$, $M_\infty = 0.73$ and $\alpha = 3.5$ deg.

Future efforts will be devoted to characterise this aspect by accounting for the effect of the non equilibrium of forces and pitching moment. Moreover, 3D wing configurations will be tested to assess the efficiency of the aforementioned methods. The position of spoilers in relation to the development of buffet along 3D wings gives hope for a successful outcome.

## Declaration of competing interest

The authors declare the following financial interests/personal relationships which may be considered as potential competing interests:

Andrea Petrocchi was supported by the European Union.

## Data availability

Data will be made available on request.

## References

[1] H.H. Pearcey, A method for the prediction of the onset of buffeting and other separation effects from wind-tunnel tests on rigid models, Tech. Rep., aGARD Report 223, 1958.
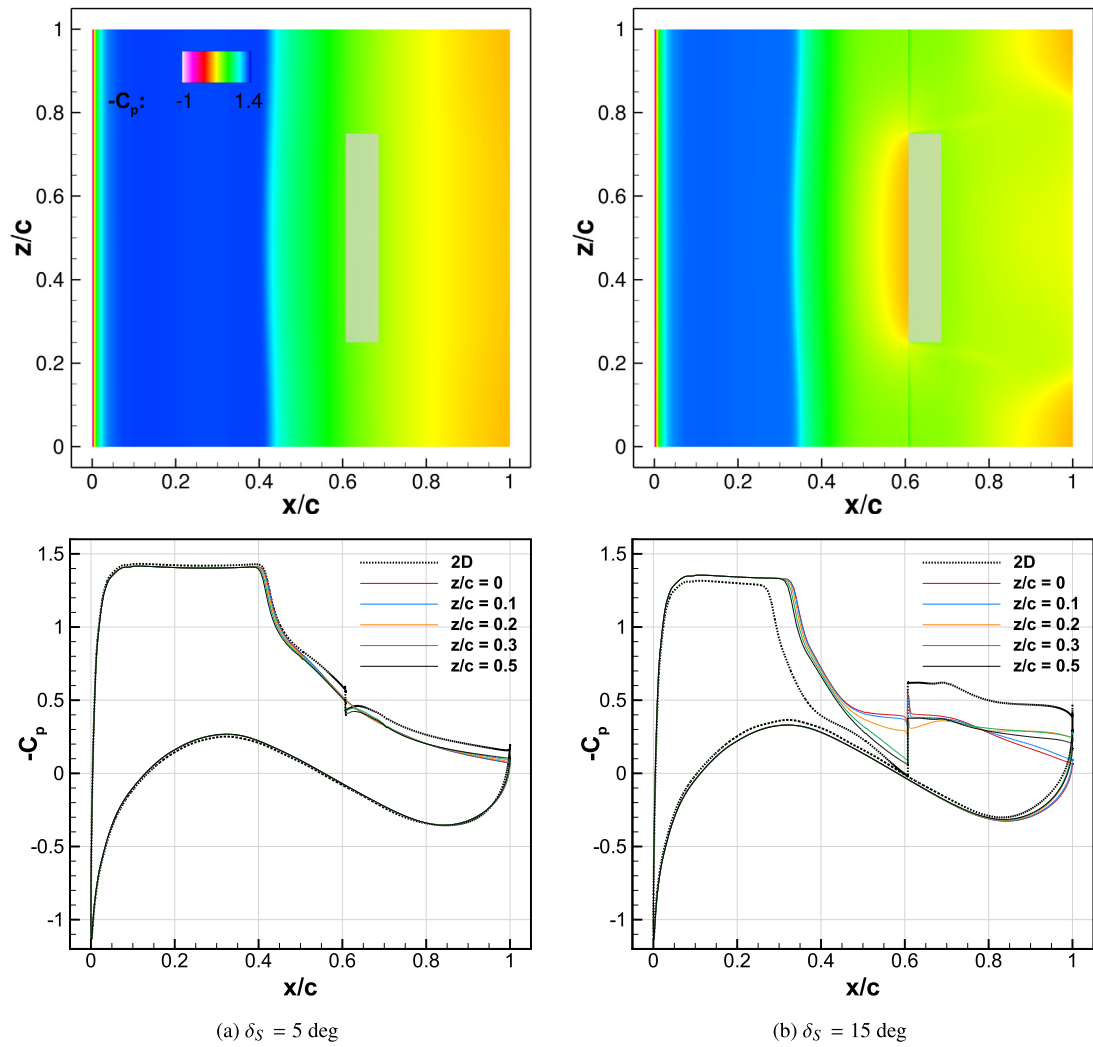
(a) $\delta_S$ = 5 deg

(b) $\delta_S$ = 15 deg

**Fig. 23.** Contours (top) and line plots at different spanwise locations (bottom) of the pressure coefficient around the OAT15A wing at $Re_c = 3 \times 10^6$, $M_\infty = 0.73$ and $\alpha = 3.5$ deg. $z/c = 0$ corresponds to the domain sidewall while $z/c = 0.5$ corresponds to the symmetry plane. Dashed, black lines indicate the results of the 2D computations at the same angles.
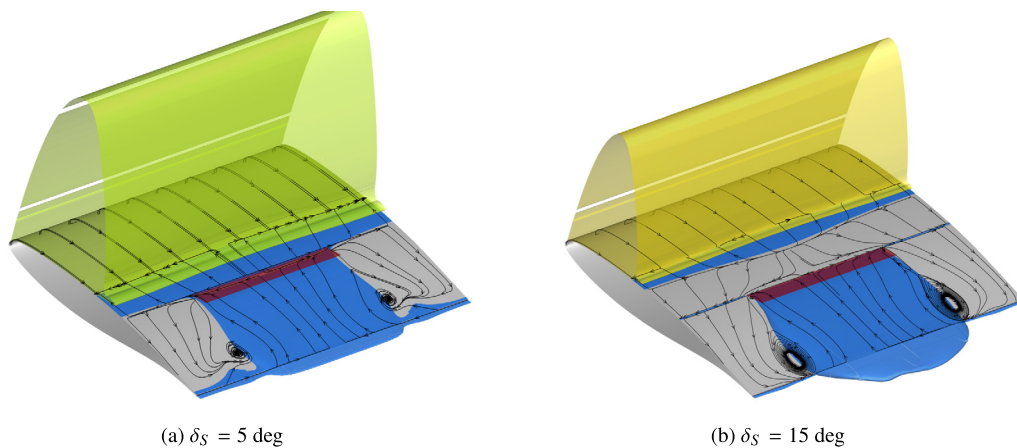


(a) $\delta_S$ = 5 deg

(b) $\delta_S$ = 15 deg

**Fig. 24.** $M_\infty = 1$ (yellow) and $U/U_0 = -0.001$ (blue) iso-surfaces for the flow around the OAT15A wing at $Re_c = 3 \times 10^6$, $M_\infty = 0.73$ and $\alpha = 3.5$ deg. The spoiler is indicated by the red surface.
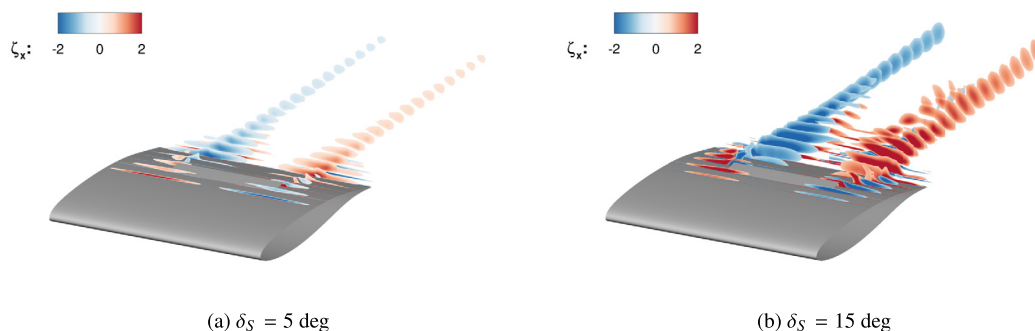
(a) $\delta_S = 5$ deg

(b) $\delta_S = 15$ deg

**Fig. 25.** Longitudinal component of the vorticity vector around the OAT15A wing at $\mathrm{Re}_c = 3 \times 10^6$, $\mathrm{M}_\infty = 0.73$ and $\alpha = 3.5$.

[2] H. Tijdeman, Investigation of the transonic flow around oscillating airfoils, Tech. Rep., National Aerospace Laborator, The Netherlands, rNLR TR 77090 U, 1977.

[3] B. Lee, Oscillatory shock motion caused by transonic shock boundary-layer interaction, AIAA J. 28 (1994) 942–944, https://doi.org/10.2514/3.25144.

[4] L. Jacquin, P. Molton, S. Deck, B. Maury, D. Soulevant, Experimental study of shock oscillation over a transonic supercritical profile, AIAA J. 47 (2009) 1985–1994, https://doi.org/10.2514/1.30190.

[5] J. Crouch, A. Gargaruk, D. Magidov, A. Travin, Origin of transonic buffet on aerofoils, J. Fluid Mech. 628 (2009) 357–369, https://doi.org/10.1017/S0022112009006673.

[6] N. Giannelis, G. Vio, O. Levinski, A review of recent developments in the understanding of transonic shock buffet, Prog. Aerosp. Sci. 92 (2017) 39–84, https://doi.org/10.1016/j.paerosci.2017.05.004.

[7] P. Molton, J. Dandois, A. Lepage, V. Brunet, R. Bur, Control of buffet phenomenon on a transonic swept wing, AIAA J. 51 (2013) 761–772, https://doi.org/10.2514/1.J051000.

[8] J. Dandois, A. Lepage, J.-B. Dor, P. Molton, F. Ternoy, A. Geeraert, V. Brunet, E. Coustols, Experimental study of transonic buffet phenomenon on a 3D swept wing, C. R., Méc. 342 (2014) 425–436, https://doi.org/10.1016/j.crme.2014.01.015.

[9] L. Masini, A. Peace, S. Timme, Influence of vane vortex generators on transonic wing buffet: further analysis of the BUCOLIC experimental dataset, in: 52nd 3AF International Conference on Applied Aerodynamics, Lyon, France, 2017.

[10] J. Birkenmeyer, H. Rosemann, E. Stanewsky, Shock control on a swept wing, Aerosp. Sci. Technol. 4 (2000) 147–156, https://doi.org/10.1016/S1270-9638(00)00128-0.

[11] R. Mayer, T. Lutz, E. Kramer, Numerical study on the ability of shock control bumps for buffet control, AIAA J. 56 (2018) 1978–1987, https://doi.org/10.2514/1.J056737.

[12] R. Mayer, T. Lutz, E. Kramer, Control of transonic buffet by shock control bumps on wing-body configuration, AIAA J. 56 (2019) 556–568, https://doi.org/10.2514/1.C034969.

[13] A. D'Aguanno, F. Schrijer, B. van Oudheusden, Investigation of 3D shock control bumps for transonic buffet alleviation, in: AIAA Aviation 2021 Forum, Virtual Event, 2021.

[14] D. Caruana, A. Mignosi, C. Robitaillié, M. Corrège, Separated flow and buffeting control, Flow Turbul. Combust. 71 (2003) 221–245, https://doi.org/10.2514/1.40932.

[15] D. Caruana, A. Mignosi, M. Corrège, A.L. Pourhiet, A. Rodde, Buffet and buffeting control in transonic flow, Aerosp. Sci. Technol. 9 (2005) 605–616, https://doi.org/10.1016/j.ast.2004.12.005.

[16] C. Gao, W. Zhang, Z. Ye, Numerical study on closed-loop control of transonic buffet suppression by trailing edge flap, Comput. Fluids 132 (2016) 32–45, https://doi.org/10.2514/2.2071.

[17] Y. Tian, Z. Li, P. Liu, Upper trailing-edge flap for transonic buffet control, J. Aircr. 55 (2018) 382–389, https://doi.org/10.2514/1.C033134.

[18] N. Titchener, H. Babinsky, A review of the use of vortex generators for mitigating shock-induced separation, Shock Waves 25 (2015) 473–494, https://doi.org/10.1007/s00193-015-0551-x.

[19] P. Bruce, S. Collins, Review of research into shock control bumps, Shock Waves 25 (2015) 451–471, https://doi.org/10.1007/s00193-014-0533-4.

[20] J. Geoghegan, N. Giannelis, G. Vio, A numerical investigation of the geometric parametrisation of shock control bumps for transonic shock oscillation control, Fluids 12 (2020) 1–29, https://doi.org/10.3390/fluids12083421.

[21] T.Y.S. Gao, P. Liu, Q. Qu, Flap upward deflection and rearward bump combination to alleviate transonic buffet of supercritical wing, in: AIAA SciTech Forum 2018, Kissimmee, FL, USA, 2018.

[22] J. Dandois, Experimental study of transonic buffet phenomenon on a 3D swept wing, Phys. Fluids 28 (2016) 1–23, https://doi.org/10.1063/1.4937426.

[23] Y. Sugioka, S. Koike, K. Nakakita, D. Numata, T. Nonomura, K. Asai, Experimental analysis of transonic buffet on a 3D swept wing using fast-response pressure-sensitive paint, Exp. Fluids 59 (2018) 1–20, https://doi.org/10.1007/s00348-018-2565-5.

[24] Y. Sugioka, K. Nakakita, S. Koike, T. Nakajima, T. Nonomura, K. Asai, Characteristic unsteady pressure field on a civil aircraft wing related to the onset of transonic buffet, Exp. Fluids 62 (2021) 20, https://doi.org/10.1007/s00348-020-03118-y.

[25] M. Iovnovich, D.E. Raveh, Numerical study of shock buffet on three-dimensional wings, AIAA J. 53 (2015) 449–463, https://doi.org/10.2514/1.J053201.

[26] Y. Ohmichi, T. Ishida, A. Hashimoto, Modal decomposition analysis of three-dimensional transonic buffet phenomenon on a swept wing, AIAA J. 56 (2018) 3938–3950, https://doi.org/10.2514/1.J056855.

[27] S. Timme, Global instability of wing shock-buffet onset, J. Fluid Mech. 885 (2020) A37, https://doi.org/10.1017/jfm.2019.1001.

[28] L. Poplingher, D. Raveh, Comparative modal study of the two-dimensional and three-dimensional transonic shock buffet, AIAA J. 61 (2023) 125–144, https://doi.org/10.2514/1.J061797.

[29] L. Masini, S. Timme, A.J. Pace, Scale-resolving simulations of a civil aircraft wing transonic shock-buffet experiment, AIAA J. 58 (2020) 4322–4338, https://doi.org/10.2514/1.J059219.

[30] A. D'Aguanno, F. Schrijer, B. van Oudheusden, Experimental characterization of upper trailing edge flaps for transonic buffet control, Flow Turbul. Combust. 110 (2023) 325–350, https://doi.org/10.1007/s10494-022-00381-3.

[31] A. Hartmann, A. Feldhusen, W. Schröder, On the interaction of shock waves and sound waves in transonic buffet, Phys. Fluids 25 (2013) 026101, https://doi.org/10.1063/1.4791603.

[32] A. Feldhusen-Hoffmann, V. Statnikov, M. Klaas, W. Schroder, Investigation of shock–acoustic-wave interaction in transonic flow, Exp. Fluids 59 (2018) 1–20, https://doi.org/10.1007/s00348-017-2466-z.

[33] J. Crouch, A. Gargaruk, D. Magidov, Predicting the onset of flow unsteadiness based on global instability, J. Comput. Phys. 224 (2007) 924–940, https://doi.org/10.1016/j.jcp.2006.10.035.

[34] J. Crouch, A. Gargaruk, M. Strelets, Global instability in the onset of transonic-wing buffet, J. Fluid Mech. 881 (2019) 3–22, https://doi.org/10.1017/jfm.2019.748.

[35] H. Babinsky, H. Ogawa, SBLI control for wings and inlets, Shock Waves 18 (2008) 89–96, https://doi.org/10.1007/s00193-008-0149-7.

[36] S. Künnecke, S. Vasista, J. Riemenschneider, R. Keimer, Review of adaptive shock control systems, Appl. Sci. 11 (2021) 817, https://doi.org/10.3390/app11020817.

[37] Y. Tian, P. Feng, P. Liu, T. Hu, Q. Qu, Spoiler upward deflection on transonic buffet control of supercritical airfoil and wing, J. Aircr. 54 (2017) 1227–1231, https://doi.org/10.2514/1.C033574.

[38] V. Pastrikakis, G. Barakos, Effect of active Gurney flaps on overall helicopter flight envelope, Aeronaut. J. 120 (2016) 1230–1261, https://doi.org/10.1017/aer.2016.57.

[39] R. Steijl, G. Barakos, K. Badcock, A framework for CFD anal-ysis of helicopter rotors in hover and forward flight, Int. J. Numer. Methods Fluids 51 (2006) 819–847, https://doi.org/10.1002/fld.1086.

[40] R. Steijl, G. Barakos, Sliding mesh algorithm for CFD analysis of helicopter rotor–fuselage aerodynamics, Int. J. Numer. Methods Fluids 58 (2008) 527–549, https://doi.org/10.1002/fld.1757.

[41] S. Osher, S. Chakravarthy, Upwind schemes and boundary conditions with applications to Euler equations in general geometries, J. Comput. Phys. 50 (1983) 447–481, https://doi.org/10.1016/0021-9991(83)90106-7.

[42] B. van Leer, Towards the ultimate conservative difference scheme. V. A second-order sequel to Godunov's method, J. Comput. Phys. 32 (1979) 101–136, https://doi.org/10.1016/0021-9991(79)90145-1.

[43] G. van Aldaba, B. van Leer, W. Roberts, A comparativestudy of computational methods in cosmic gas dynamics, Astron. Astrophys. 108 (1982) 76–84.

[44] A. Jameson, Time-dependent calculations using multigrid, with applications to unsteady flows past airfoils and wings, in: AIAA 10th Computational Fluid Dynamics Conference, 1991.

[45] O. Axelsson, Iterative Solution Methods, Cambridge University Press, 1994.

[46] S. Girimaji, K. Abdol-Hamid, Partially-averaged Navier Stokes model for turbulence: implementation and validation, in: AIAA Aerospace Sciences Meeting and Exhibit, Reno, NE, USA, 2005.

[47] D.C. Wilcox, Formulation of the $k - \omega$ turbulence model revisited, AIAA J. 46 (2008) 2823–2838, https://doi.org/10.2514/1.36541.

[48] S. Lakshimpathy, S. Girimaji, Partially-averaged Navier Stokes method for turbulent flows: $k - \omega$ model implementation, in: AIAA Aerospace Sciences Meeting and Exhibit, Reno, NE, USA, 2006.

[49] F. Menter, Two-equation eddy-viscosity turbulence models for engineering applications, AIAA J. 32 (1994) 1598–1605, https://doi.org/10.2514/3.121495.

[50] D. Luo, C. Yan, X. Wang, Computational study of supersonic turbulent-separated flows using partially averaged Navier-Stokes method, Acta Astronaut. 107 (2015) 234–246, https://doi.org/10.1016/j.actaastro.2014.11.029.

[51] M.A. Woodgate, V.A. Pastrikakis, G.N. Barakos, Rotor computations with active Gurney flaps, in: M. Braza, A. Bottaro, M. Thompson (Eds.), Advances in Fluid-Structure Interaction, Springer International Publishing, 2016, pp. 133–166.

[52] L. Jacquin, P. Molton, S. Deck, B. Maury, D. Soulevant, An experimental study of shock oscillation over a transonic supercritical profile, in: AIAA Aerospace Sciences Meeting and Exhibit, Toronto, Ontario, Canada, 2005.

[53] J. McDevitt, A.F. Okuno, Static and dynamic pressure measurements on a NACA 0012 airfoil in the Ames high Reynolds number facility, Tech. rep., National Aeronautics and Space Administration, nASA-TP-2485, 1985.

[54] F. Billard, T. Davidson, H. Babinsky, R. Placek, M. Miller, P. Ruchała, W. Stryczniewicz, T. Kwiatkowski, W. Stalewski, J. Sznajder, S. Kuprianowicz, M. Bernardini, S. Pirozzoli, G. Barakos, G. Zografakis, B. Tartinville, C. Hirsch, D. Szubert, M. Braza, I. Asproulias, N. Simiriotis, J.-B. Tô, Y. Hoarau, WP-5 External Flows—Wing, Springer International Publishing, Cham, 2021, pp. 347–512.

[55] M. Iovnovich, D.E. Raveh, Reynolds-averaged Navier–Stokes study of the shock-buffet instability mechanism, AIAA J. 50 (2012) 880–890, https://doi.org/10.2514/1.J051329.

[56] F. Grossi, M. Braza, Y. Hoarau, Prediction of transonic buffet by delayed detached-eddy simulation, AIAA J. 52 (2014) 2300–2312, https://doi.org/10.2514/1.J052873.

[57] A. Petrocchi, G. Barakos, Buffet boundary estimation using a harmonic balance method, Aerosp. Sci. Technol. 132 (2023) 108086, https://doi.org/10.1016/j.ast.2022.108086.

[58] A. Petrocchi, G.N. Barakos, Transonic buffet simulation using a partially-averaged Navier-Stokes approach, in: ECCOMAS 2022, Oslo, Norway, 2022.

[59] S. Scharnowski, K. Kokmanian, C. Schafer, T. Baur, A. Accorinti, C.J. Kahler, Shock-buffet analysis on a supercritical airfoil with a pitching degree of freedom, Exp. Fluids 63 (2022) 93, https://doi.org/10.1007/s00348-022-03427-4.